

# Optical, microphysical and radiative properties of aerosols over a tropical rural site in Kenya, East Africa: Source identification, modification and aerosol type discrimination

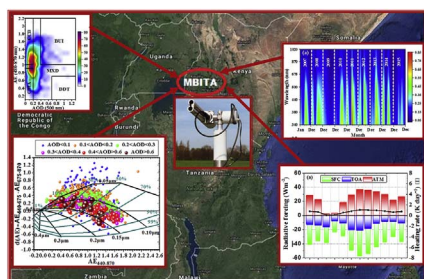
Richard Boiyo<sup>a,b</sup>, K. Raghavendra Kumar<sup>a,\*</sup>, Tianliang Zhao<sup>a,\*\*</sup>

<sup>a</sup> Collaborative Innovation Centre on Forecast and Evaluation of Meteorological Disasters, Key Laboratory of Meteorological Disaster, Ministry of Education (KLME), International Joint Laboratory on Climate and Environment Change (ILCEC), Key Laboratory for Aerosol-Cloud-Precipitation of China Meteorological Administration, School of Atmospheric Physics, Nanjing University of Information Science and Technology, Nanjing 210044, Jiangsu, China

<sup>b</sup> Department of Physical Sciences, Meru University of Science and Technology, P.O. Box 972-60200, Meru, Kenya



## GRAPHICAL ABSTRACT



## ARTICLE INFO

### Keywords:

AERONET  
AOD  
SSA  
Aerosol-type classification  
Radiative forcing  
East Africa

## ABSTRACT

A better understanding of aerosol optical, microphysical and radiative properties is a crucial challenge for climate change studies. In the present study, column-integrated aerosol optical and radiative properties observed at a rural site, Mbita (0.42°S, 34.20°E, and 1125 m above sea level) located in Kenya, East Africa (EA) are investigated using ground-based Aerosol Robotic Network (AERONET) data retrieved during January, 2007 to December, 2015. The annual mean aerosol optical depth ( $AOD_{500\text{ nm}}$ ), Ångström exponent ( $AE_{440-870\text{ nm}}$ ), fine mode fraction of  $AOD_{500\text{ nm}}$  ( $FMF_{500\text{ nm}}$ ), and columnar water vapor (CWV, cm) were found to be  $0.23 \pm 0.08$ ,  $1.01 \pm 0.16$ ,  $0.60 \pm 0.07$ , and  $2.72 \pm 0.20$ , respectively. The aerosol optical properties exhibited a unimodal distribution with substantial seasonal heterogeneity in their peak values being low (high) during the local wet (dry) seasons. The observed data showed that Mbita and its environs are significantly influenced by various types of aerosols, with biomass burning and/or urban-industrial (BUI), mixed (MXD), and desert dust (DDT) aerosol types contributing to 37.72%, 32.81%, and 1.40%, respectively during the local dry season (JJA). The aerosol volume size distribution (VSD) exhibited bimodal lognormal structure with a geometric mean radius of  $0.15\text{ }\mu\text{m}$  and  $3.86\text{--}5.06\text{ }\mu\text{m}$  for fine- and coarse-mode aerosols, respectively. Further, analysis of single scattering albedo (SSA), asymmetry parameter (ASY) and refractive index (RI) revealed dominance of fine-mode absorbing aerosols during JJA. The averaged aerosol direct radiative forcing (ARF) retrieved from the AERONET showed a strong cooling effect at the bottom of the atmosphere (BOA) and significant warming within the atmosphere (ATM), representing the important role of aerosols played in this rural site of Kenya. Finally, the Hybrid Single

\* Corresponding author.

\*\* Corresponding author.

E-mail addresses: [rkumar@nuist.edu.cn](mailto:rkumar@nuist.edu.cn) (K.R. Kumar), [tlzhao@nuist.edu.cn](mailto:tlzhao@nuist.edu.cn) (T. Zhao).

Particle Lagrangian Integrated Trajectory (HYSPPLIT) model revealed that aerosols from distinct sources resulted in enhanced loading during JJA.

## 1. Introduction

Atmospheric aerosols are an inevitable topic in Atmospheric Physics and Chemistry (Kalluri et al., 2016). They consist of solid or liquid particles suspended in the atmosphere with sizes ranging from a few nanometers to tens of microns. Although they constitute a small fraction of the atmosphere, they are among the major climate forcing agents recognized globally (Zhang and Reid, 2010; IPCC, 2013). They affect climate directly by scattering and absorbing solar radiation, thereby, altering radiation budget at the top, bottom and within the atmosphere which in turn influences the atmospheric heating rate (Charlson et al., 1992). They also modify the optical and microphysical properties of clouds, including their lifetime, formation and precipitation, and therefore, indirectly change terrestrial radiation (Ramanathan et al., 2001). Aerosols also have detrimental effects on human health, air quality and visibility (Gauderman et al., 2002; McMichael et al., 2006; Liao et al., 2015; Yu et al., 2016a).

Despite of the considerable progress made in understanding atmospheric aerosols and their climatic impacts, aerosol radiative forcing (ARF) remains one of the largest uncertainties in climate change studies (IPCC, 2013; Patel et al., 2017a, b; Bibi et al., 2017). This is partly because of incomplete knowledge of aerosol's spatiotemporal variability and their associated properties (Alam et al., 2011; Kumar et al., 2014, 2015; Boiyo et al., 2017a). A good understanding of aerosol's spatio-temporal variability in terms of abundance, optical, microphysical and radiative properties is, therefore, needed to improve our scientific understanding of their sources (natural and anthropogenic) and sinks, and to provide adequate information for policy making (Zhang and Reid, 2010). In this regard, a number of ways ranging from field measurements (Moorthy et al., 2005), ground- (Holben et al., 1998) to satellite-based remote sensing (Remer et al., 2005; Kahn et al., 2005; Kang et al., 2016a), have been designed to monitor aerosols over different parts of

the globe. Ground-based remote sensing networks such as Aerosol Robotic Network (AERONET; Holben et al., 1998), European Aerosol Research Lidar Network (EARLINET; Amiridis et al., 2005), Micro-Pulse Lidar Network (MPLNET; Welton and Campbell, 2002) and China Aerosol Remote Sensing Network (CARSNET; Che et al., 2009) procure continuous datasets at multiple wavelengths to characterize aerosol optical, microphysical and radiative properties.

Several studies utilizing such networks have been reported in various parts of the globe (Alam et al., 2011, 2012; More et al., 2013; Adesina et al., 2014, 2017; Cheng et al., 2015; Kang et al., 2016b; Yu et al., 2016b; Patel et al., 2017a,b; Kumar et al., 2017; Bibi et al., 2016, 2017). Using ground-based AERONET data over the Nation Capital Region Delhi (India), Kumar et al. (2016) reported change in ARF from  $21.2 \text{ W m}^{-2}$  to  $56.6 \text{ W m}^{-2}$  for clean and polluted environments, respectively. Studies by Alam et al. (2012) and Bibi et al. (2016, 2017) at Karachi and Lahore (Pakistan) reported significant seasonal heterogeneity in ARF attributed to seasonal cycles of emission sources and meteorological variables. At Granada (Spain), Lyamani et al. (2009) noticed large fraction of absorbing aerosols; while Esteve et al. (2014) reported mean ARF values of  $-17 \pm 1.0 \text{ W m}^{-2}$  and  $-2.2 \pm 1.3 \text{ W m}^{-2}$  at the bottom (BOA) and top of the atmosphere (TOA), respectively over Burjassot (Spain). Studies by Ogunjobi et al. (2008) and El-Metwally et al. (2011) reported a wide range of aerosol loading over various AERONET sites in West Africa and Cairo (Egypt) during 2003–2005 and 2004–2006, respectively. Recently, Adesina et al. (2017) and Kumar et al. (2017) reported significant heating within the atmosphere due to absorbing aerosols over selected AERONET sites in South Africa. In other related studies, Makokha and Angeyo (2013) reported invariant values of ARF over three AERONET sites in Kenya using the Coupled Ocean and Atmosphere Radiative Transfer (COART) model.

ARF at local and regional scales can exceed global values by an

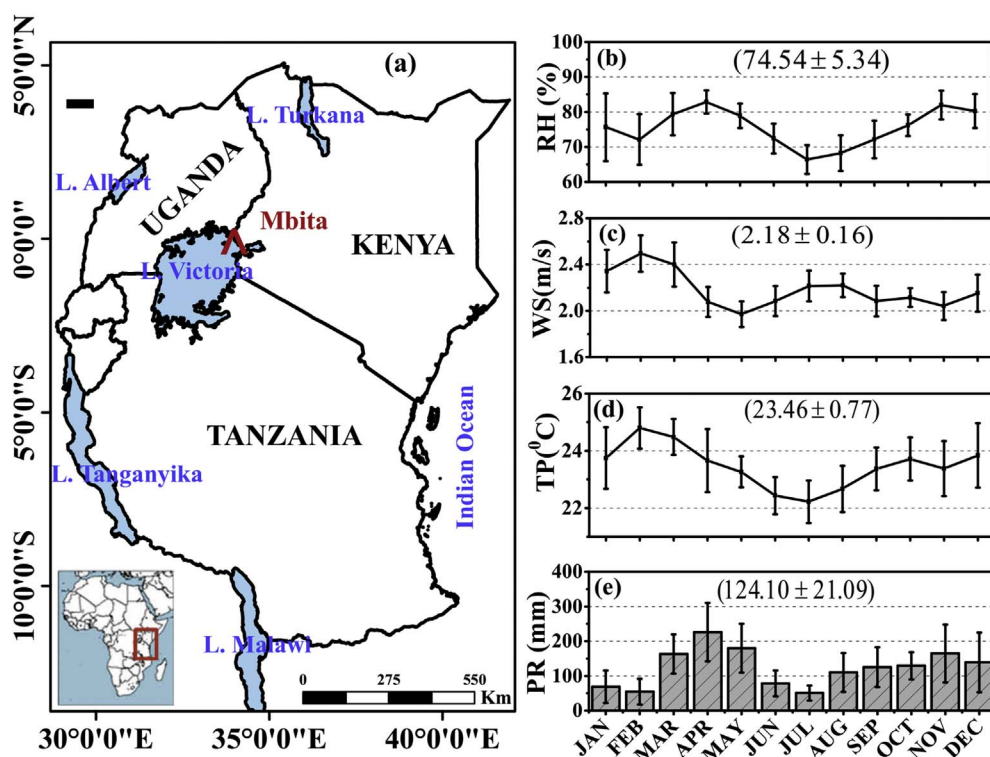


Fig. 1. (a) Map of East Africa over African continent (inset) showing geographical location of Mbita. Monthly mean ( $\pm \sigma$ ) variations in surface meteorological variables: (b) relative humidity (RH; %), wind speed (WS; m/s), temperature (TP; °C), and precipitation (PR; mm) observed at Mbita during 2001–2015. The numerals enclosed within brackets in panels b–e corresponds to the annual mean along with the respective standard deviation.

order of magnitude due to large influence of local sources, aerosol properties, and removal processes (Esteve et al., 2014). It is, therefore, important that we obtain accurate and detailed information on ARF over different regions of the globe, particularly unique and least studied ones such as East Africa (EA) (Boiyo et al., 2017a, b). Despite of the valuable ground-based AERONET data, EA suffers from inadequate characterization of aerosols especially the optical, microphysical and radiative properties with far reaching consequences on its inability to quantify ARF precisely. Previous studies over the region (de Graaf et al., 2010; Makokha and Angeyo, 2013; Ngaina and Muthama, 2014; Boiyo et al., 2017a, b) indicated existence of fine- and coarse-mode aerosols from various natural and anthropogenic sources resulting in varying concentrations at different spatiotemporal scales. However, basic knowledge of key aerosol types (e.g., desert dust, biomass burning, and urban-industrial) and their modification processes, which are essential in reducing uncertainties in ARF estimates (IPCC, 2013) is largely unknown. Also, investigation of other key aerosol optical (e.g., single scattering albedo; SSA, asymmetry parameter; ASY), microphysical (aerosol volume size distribution; VSD, refractive index; RI) and radiative properties which are crucial in reducing uncertainties in ARF (Cheng et al., 2015; Kang et al., 2016b; Tiwari et al., 2016; Patel et al., 2017a; Kumar et al., 2017; Adesina et al., 2017; Bibi et al., 2017) is non-existent.

In view of the immense local and regional importance of aerosols, the present study seeks to investigate the aerosol's optical, microphysical and radiative properties over Mbita, a tropical rural site located along the shores of Lake Victoria in East Africa. The study utilized 9 years (January, 2007 to December, 2015) of Level 2.0 (high quality cloud-screened and quality assured) data derived from Cimel Sun photometer (CE-318) to examine (i) temporal and spectral variability of direct sun retrievals, and their frequency distributions, (ii) curvature effect on wavelength dependence of aerosol optical depth (AOD) and Ångström exponent (AE) (iii) aerosol classification and modification processes, (iv) optical, microphysical and radiative properties of aerosols and their spectral dependencies, and (v) source identification and possible aerosol transport pathways via., the Hybrid Single Particle Lagrangian Integrated Trajectory (HYSPLIT) model. The results derived from the present work gives sense of columnar aerosol characteristics in a tropical remote site of Kenya, East Africa, and could increase the accuracy of model simulations to study climatic changes over the region. The rest of this paper is structured as follows: Section 2 describes the study area and prevailing meteorological conditions, Section 3 outlines data and methodology related to the present work. Results and discussions are elucidated in Section 4, while Section 5 illustrates the main conclusions drawn from the present work.

## 2. Study region and meteorology

### 2.1. Site description

The AERONET's aerosol observational site namely, ICIPE\_Mbita (hereafter simply, Mbita; 0.42°S, 34.20°E, 1125 m asl) is a tropical rural site located along the shores of Lake Victoria near the southwestern border of Kenya in EA (see Fig. 1a). Climatologically, the area experiences tropical weather with four seasons categorized according to precipitation patterns (Ongoma and Chen, 2017). The local wet seasons (March–April–May; MAM and September–October–November; SON) experience low AODs due to enhanced wet scavenging and reduced anthropogenic activities. On the other hand, high AODs characterize local dry seasons (June–July–August; JJA and December–January–February; DJF) attributed to change in meteorological conditions and emission sources (de Graaf et al., 2010; Makokha and Angeyo, 2013; Boiyo et al., 2017a, b). The main local sources of aerosols around the site include biomass burning from neighboring agricultural zones and industrial-vehicular emissions due to its closer proximity to major highways and urbanized regions (Makokha and Angeyo, 2013; Boiyo

et al., 2017b). In addition, aerosols transported remotely towards the site at certain times of the year could significantly influence the loading.

### 2.2. Local climatology

Apart from the aerosol data, the study also employed monthly mean meteorological parameters for air temperature (TP; °C), wind speed (WS;  $\text{ms}^{-1}$ ), relative humidity (RH; %), and precipitation (PR; mm) to examine prevailing climatic condition over Mbita. The wind speed and relative humidity datasets at  $0.75^\circ \times 0.75^\circ$  spatial resolution were sourced from European Centre for Medium-Range Weather Forecasts (ECMWF) previously used by a number of authors (Yang et al., 2015; Ogwang et al., 2016; Boiyo et al., 2017b) over EA. However, the Climate Research Unit (CRU) temperature and Tropical Rainfall Measuring Mission (TRMM) (Huffman et al., 2007) precipitation datasets at spatial resolutions of  $0.5^\circ \times 0.5^\circ$  and  $0.25^\circ \times 0.25^\circ$ , respectively were preferred due to their better performance over the region (Yang et al., 2015; Kerandi et al., 2017). These meteorological datasets were retrieved at 850 hPa (except precipitation) during January, 2001 to December, 2015.

Fig. 1b and e shows the monthly mean ( $\pm \sigma$ ) climatology of different meteorological parameters observed at Mbita during January, 2001 to December, 2015. The mean RH ranged from  $66.39 \pm 4.13\%$  in July to  $82.87 \pm 3.34\%$  in April (Fig. 1b); while the mean WS varied between  $1.97 \pm 0.11 \text{ ms}^{-1}$  in May and  $2.49 \pm 0.16 \text{ ms}^{-1}$  in February (Fig. 1c). Ambient air temperature was noticed to be the highest in February ( $24.80 \pm 0.72^\circ\text{C}$ ) during the first local dry season, and systematically decreases to a minimum value in July ( $22.22 \pm 0.74^\circ\text{C}$ ) during the second local dry season (Fig. 1d). Like most parts of EA, Mbita and its environs receive bimodal precipitation patterns (Fig. 1e). With a total annual precipitation of 1489.20 mm, the study location receives maximum precipitation in April ( $225.94 \pm 84.17 \text{ mm}$ ) and November ( $164.47 \pm 83.02 \text{ mm}$ ), and minimum in July ( $50.91 \pm 21.54 \text{ mm}$ ) and February ( $54.95 \pm 36.91 \text{ mm}$ ). In this paper, the aerosol properties are analyzed for four major seasons (MAM, JJA, SON, and DJF) based on precipitation patterns (Ongoma and Chen, 2017).

## 3. Data and methods

### 3.1. Direct and inversion products

The remotely-sensed ground-based aerosol data utilized in this study were conducted by the Cimel Sun photometer (CE-318) established and maintained by NASA (Holben et al., 1998). The radiometers collect measurements of direct sun and diffuse sky radiances in 15 and 30 min interval between the spectral ranges of 340–1640 nm and 440–1020 nm, respectively, with a  $1.2^\circ$  field of view (Holben et al., 1998). Two versions: Versions 1 and 2 and three quality levels: Level 1.0 (cloud contaminated), Level 1.5 (cloud screened), and Level 2.0 (cloud screened and quality-assured) are provided. The high quality Version 2, Level 2.0 direct sun products of AOD (at 340, 380, 440, 500, 675, 870, 940 and 1020 nm), column water vapor (CWV) (940 nm), and AE (440–870 nm) were used in the present study. Besides these, the inversion products retrieved from spectral sun and sky observations (Dubovik et al., 2000) at 440, 675, 870 and 1020 nm were also utilized. They include, column-integrated aerosol volume size distribution (VSD) estimated at 22 radius size bins ranging from 0.05 to  $15 \mu\text{m}$ , the real (Re) and imaginary (Im) parts of the aerosol refractive index (RI), the asymmetry parameter (ASY) and single scattering albedo (SSA). The AERONET inversion algorithm also estimates ARF using the DIScrete Ordinate Radiative Transfer (DISORT) module provided with the retrieved inputs of inversion products (Kumar et al., 2017; Adesina et al., 2017). In addition to ARF, the aerosol radiative forcing efficiency (ARFE) values were also obtained from the AERONET inversion

algorithm. All these data products were retrieved and downloaded at <http://aeronet.gsfc.nasa.gov> for the study period January, 2007 to December, 2015. Details concerning instrumentation, data acquisition, retrieval algorithms and calibration procedures have been described by several previous authors (Holben et al., 1998, 2001; Dubovik et al., 2000; Dubovik et al., 2002; Smirnov et al., 2002; Alam et al., 2012; Kumar et al., 2013; Tiwari et al., 2016; Yu et al., 2016b; Patel et al., 2017a; Bibi et al., 2017).

Tables 1–3 summarize statistics of Level 2.0 data counts used in the present study. A total of 1841 daily data points (from 44210 instantaneous data points) of direct sun observations were considered in this work. In addition, the instrument collected 169 daily values of SSA and RI, and 877 values of ASY and VSD. Notably, the direct sun products were significantly larger than the inversion products. This is because the aerosol information content is limited under background condition, so the inversion products are restricted and available only when  $\text{AOD}_{440\text{ nm}} > 0.4$  (Cheng et al., 2015; Patel et al., 2017b and references therein). At Mbita, the enhanced precipitation during local wet seasons (Fig. 1e) enhanced wet deposition processes, resulting to low turbid conditions. Therefore, limited scans were satisfied gives  $\text{AOD}_{440\text{ nm}} > 0.4$ .

### 3.2. Methods

#### 3.2.1. Ångström exponent and its derivative

The spectral dependence of AOD is well represented by the Ångström power law (Ångström, 1961) (Eq. (1));

$$\tau_\lambda = \beta\lambda^{-\alpha} \quad (1)$$

where  $\tau_\lambda$  is the estimated AOD at wavelength  $\lambda$  ( $\mu\text{m}$ ). The Ångström turbidity coefficient ( $\beta$ ) varied in the range 0–1 acts as an indicator of the amount of aerosols present in the atmosphere, being equal to  $\tau_\lambda$  at  $\lambda = 1\mu\text{m}$ . The spectrally averaged Ångström exponent ( $\alpha$  or AE), which is inversely related to amount of aerosol particles, provides useful information about particle-size. It is a good indicator of the fraction of fine- (0.1–1  $\mu\text{m}$ ) to coarse- (> 1  $\mu\text{m}$ ) mode particles (Kumar et al., 2013; Patel et al., 2017a; Adesina et al., 2017). Higher (> 1) values of AE indicate relatively high ratios of fine- relative to coarse-mode particles associated with urban pollution, combustion of by-products (e.g., smoke particles resulting from biomass burning and sulfates). On the other hand, lower (< 1) values of AE indicate predominance of coarse-relative to fine-mode particles, typically associated with sea salt and desert dust (Eck et al., 2010; Patel et al., 2017b). In the present study, was estimated in the range 440–870 nm, 440–675 nm and 675–870 nm following Eq. (2);

$$\alpha = -\frac{d \ln \tau_\lambda}{d \ln \lambda} = \frac{\ln\left(\frac{\tau_{\lambda_1}}{\tau_{\lambda_2}}\right)}{\ln\left(\frac{\lambda_1}{\lambda_2}\right)} \quad (2)$$

where  $\tau_{\lambda_1}$  and  $\tau_{\lambda_2}$  represent AOD at wavelengths  $\lambda_1$  and  $\lambda_2$ , respectively.

AE is related to the Junge or Power Law size distribution (Eck et al., 2010). However, the size distributions of aerosols typically neither do not follow the Junge distribution nor have radii extending from zero to infinity. Therefore, the departure from these conditions often introduces a curvature in the  $\ln \tau_\lambda$  versus  $\ln \lambda$  relationship, which can be described by the second-order polynomial fit given in Eq. (3).

$$\ln \tau_\lambda = a_2 (\ln \lambda)^2 + a_1 (\ln \lambda) + a_0 \quad (3)$$

where  $a_0$ ,  $a_1$  and  $a_2$  are the coefficients obtained from the second-order polynomial fit. The coefficient  $a_2$  accounts for the spectral curvature effects, with negative (positive) values indicating aerosol size distributions dominated by fine (coarse) mode particles (Kaskaoutis et al., 2007; Kumar et al., 2013; Kang et al., 2016b; Yu et al., 2016b; Patel et al., 2017a).

The second-order polynomial fit (Eq. (3)) was applied to AOD values at six wavelengths (340, 380, 440, 500, 675 and 870 nm). AODs at 1020 nm were not used since the wavelength is affected by CWV (Kumar et al., 2013; Kang et al., 2016b). Although the polynomial fit (Eq. (3)) is more precise than the linear fit (Eq. (2)), large errors can appear especially under low turbid conditions. The derivation of AE with respect to  $\ln \lambda$  implies:

$$\frac{d\alpha}{d \ln \lambda} = \alpha' = -2a_2 \quad (4)$$

In this work, values of  $\alpha'$  were derived using the AERONET AODs measured at 340, 380, 440, 500, 675, and 870 nm. Positive values of  $\alpha'$  indicate abundance of fine-mode particles in the size-distribution; whereas, near zero or negative values were used as a surrogate for coarse-mode relative to fine-mode aerosols (Eck et al., 1999).

#### 3.2.2. Estimation of aerosol radiative forcing, efficiency, and heating rate

The ARF ( $\text{Wm}^{-2}$ ) at the TOA (100 km) and BOA (1 km) is calculated as the difference between the net solar fluxes with and without aerosols (Eq. (5)) (Dumka et al., 2014; Adesina et al., 2017).

$$\Delta F = (F_{a1} - F_{a1}) - (F_{o1} - F_{o1}) \quad (5)$$

where  $\Delta F$  is the net radiation (downwelling minus upwelling; in  $\text{W m}^{-2}$ ), while  $F_a$  and  $F_o$  denote the global irradiances with and without aerosols, respectively either at the TOA or BOA. The arrows indicate direction of global irradiances (down ↓ and up ↑). Negative values of ARF correspond to an aerosol cooling effect; whereas, positive ones correspond to a warming effect (Dumka et al., 2014; Adesina et al., 2017; Kumar et al., 2017). The net atmospheric forcing (ATM) was

**Table 1**  
The statistics of level 2.0 direct Sun all points format data for AOD, AE and CWV measured at Mbita.

Month	Number of days										Number of instantaneous data									
	2007	2008	2009	2010	2011	2012	2013	2014	2015	Total	2007	2008	2009	2010	2011	2012	2013	2014	2015	Total
Jan	26	6	0	5	29	2	22	22	0	112	1009	96	0	58	712	16	346	546	0	2783
Feb	22	27	0	4	25	0	22	26	0	126	724	859	0	44	755	0	406	479	0	3267
Mar	31	26	0	21	28	21	15	26	0	168	999	867	0	501	849	768	234	661	0	4879
Apr	25	12	0	21	29	11	0	10	12	120	550	257	0	307	1130	218	0	275	243	2980
May	28	13	0	21	24	5	22	1	23	137	785	384	0	205	621	85	805	17	637	3539
Jun	27	27	0	24	19	15	28	18	27	185	615	771	0	547	364	261	1050	265	535	4408
Jul	26	28	0	29	19	21	29	31	28	211	716	557	0	754	559	397	961	822	653	5419
Aug	28	4	0	26	25	24	25	12	31	175	978	52	0	421	480	494	607	184	736	3952
Sep	29	0	0	24	25	30	23	5	28	164	798	0	0	466	524	797	716	146	715	4162
Oct	26	0	10	30	25	28	2	0	26	147	771	0	127	626	538	651	75	0	416	3204
Nov	22	0	26	24	24	26	26	0	19	167	530	0	491	423	382	599	407	0	295	3127
Dec	2	0	17	30	29	16	18	0	17	129	30	0	315	734	583	231	380	0	217	2490
Total	292	143	53	259	301	199	232	151	211	1841	8505	3843	933	5086	7497	4517	5987	3395	4447	44210



**Table 2**

The statistics of level 2.0 sky inversion (almucantar retrievals) all points format data for SSA and RI. For ASY and VSD, the statistics are given in the following continuation table.

Month	Number of days										Number of instantaneous data									
	2007	2008	2009	2010	2011	2012	2013	2014	2015	Total	2007	2008	2009	2010	2011	2012	2013	2014	2015	Total
Jan	2	0	0	0	3	0	0	0	0	5	2	0	0	0	6	0	0	0	0	8
Feb	1	1	0	0	2	0	0	0	0	4	2	2	0	0	2	0	0	0	0	6
Mar	0	0	0	0	0	1	0	0	0	1	0	0	0	0	0	1	0	0	0	1
Apr	0	0	0	0	0	0	0	0	0	0	0	0	0	0	0	0	0	0	0	0
May	0	0	0	0	0	0	0	0	0	0	0	0	0	0	0	0	0	0	0	0
Jun	5	2	0	0	6	0	2	0	1	16	16	2	0	0	11	0	2	0	1	32
Jul	10	2	0	6	4	0	12	6	3	43	40	2	0	11	10	0	15	7	6	91
Aug	3	0	0	7	3	0	0	1	0	14	5	0	0	16	5	0	0	1	0	27
Sep	0	0	0	0	0	0	1	0	0	1	0	0	0	0	0	0	1	0	0	1
Oct	0	0	0	0	0	0	0	0	0	0	0	0	0	0	0	0	0	0	0	0
Nov	0	0	0	0	0	0	0	0	0	0	0	0	0	0	0	0	0	0	0	0
Dec	0	0	1	2	0	0	0	0	0	3	0	0	1	2	0	0	0	0	0	3
<b>Total</b>	<b>21</b>	<b>5</b>	<b>1</b>	<b>15</b>	<b>18</b>	<b>1</b>	<b>15</b>	<b>7</b>	<b>4</b>	<b>87</b>	<b>65</b>	<b>6</b>	<b>1</b>	<b>29</b>	<b>34</b>	<b>1</b>	<b>18</b>	<b>8</b>	<b>7</b>	<b>169</b>
Jan	19	1	0	1	10	0	4	1	0	36	77	1	0	1	26	0	6	1	0	112
Feb	11	9	0	0	12	0	2	1	0	35	27	20	0	7	23	0	3	1	0	81
Mar	13	5	0	0	7	9	3	6	0	43	32	15	0	0	10	16	3	10	0	86
Apr	1	1	0	0	5	2	0	3	2	14	7	1	0	0	16	3	0	4	2	33
May	8	1	0	0	1	0	4	0	3	17	16	4	0	0	1	0	10	0	8	39
Jun	11	13	0	5	8	0	6	3	5	51	26	28	0	0	13	0	10	12	5	94
Jul	20	11	0	14	10	0	14	14	8	91	59	15	0	25	22	0	27	32	14	194
Aug	10	1	0	11	9	0	2	2	6	41	21	2	0	22	16	0	4	4	7	76
Sep	6	0	0	8	5	0	2	2	3	26	13	0	0	16	7	0	2	3	4	45
Oct	8	0	0	5	3	0	1	0	2	19	16	0	0	9	3	0	2	0	3	33
Nov	5	0	7	5	3	0	0	0	4	24	9	0	11	11	6	0	0	0	4	41
Dec	0	0	4	13	3	0	0	0	3	23	0	0	6	31	3	0	0	0	3	43
<b>Total</b>	<b>112</b>	<b>42</b>	<b>11</b>	<b>62</b>	<b>76</b>	<b>11</b>	<b>38</b>	<b>32</b>	<b>36</b>	<b>420</b>	<b>303</b>	<b>86</b>	<b>17</b>	<b>122</b>	<b>146</b>	<b>19</b>	<b>67</b>	<b>67</b>	<b>50</b>	<b>877</b>

obtained as the difference between the TOA and BOA forcing.

The atmospheric heating rate (AHR) due to absorption of solar radiation by aerosols within the atmosphere (ATM) is estimated from the first law of thermodynamics and hydrostatic equilibrium following Eq. (6) given by Liou (2002).

$$\frac{\partial T}{\partial t} = \frac{g}{C_p} \times \frac{\Delta F}{\Delta P} \times 24(\text{hr/day}) \times 3600(\text{sec/hr}) \quad (6)$$

where  $\frac{\partial T}{\partial t}$  (K day<sup>-1</sup>) is the AHR,  $\frac{g}{C_p}$  is the lapse rate, with  $g$  being the acceleration due to gravity (9.8 ms<sup>-2</sup>) and  $C_p$  the specific heat capacity of air at constant pressure (1006 Jkg<sup>-1</sup>K<sup>-1</sup>).  $\Delta P$  is the atmospheric pressure difference between the top and bottom boundaries of the atmosphere with significant amount of aerosols, and was taken as 300 hPa (Pathak et al., 2010; Patel et al., 2017a). This is attributed to the fact that the large amounts of aerosols which contribute to the atmospheric heating are usually present in the lower atmosphere (Pathak et al., 2010).

### 3.2.3. Discrimination of aerosol types

An investigation of major aerosol types found over EA was carried out via., the AOD<sub>500 nm</sub> versus AE<sub>440–870 nm</sub> relationship previously used in a number of studies (Kaskaoutis et al., 2009, 2011; Kumar et al., 2015; Patel et al., 2017a). The method is based on the sensitivity of the two wavelength dependent parameters to different microphysical properties of aerosols. Notably, the AE<sub>440–870 nm</sub> depends on aerosol particle-size, while AOD<sub>500 nm</sub> depends mainly on the aerosol column density. Therefore, the AOD<sub>500 nm</sub> versus AE<sub>440–870 nm</sub> plot qualitatively indicates the amount and dimension of the aerosols observed. In this study, contour maps were constructed using steps of 0.1 for both daily averaged values of AOD<sub>500 nm</sub> and AE<sub>440–870 nm</sub>. Different aerosol types were discriminated through determination of physically interpretable cluster regions separated by solid lines that acts as relative threshold values of AOD<sub>500 nm</sub> and AE<sub>440–870 nm</sub>. The selection of the threshold values for distinguishing different aerosol types is very important and varies depending on the geographical locations (Pace et al., 2006; Kaskaoutis et al., 2007, 2009; Patel et al., 2017a).

In the present work, AOD<sub>500 nm</sub> and AE<sub>440–870 nm</sub> values were in the range 0.01–1.3 and 0.2–2.1, respectively. Therefore, (i) values of AOD<sub>500 nm</sub> < 0.2 and AE<sub>440–870 nm</sub> < 0.9 represented as clean maritime aerosols (CMA), (ii) AOD<sub>500 nm</sub> < 0.2 and AE<sub>440–870 nm</sub> > 1.0 was used for continental clean aerosols representing background conditions (CCB) over Mbita, (iii) AOD<sub>500 nm</sub> > 0.3 and AE<sub>440–870 nm</sub> > 1.0 characterized biomass burning/urban-industrial (BUI), while (iv) AOD<sub>500 nm</sub> values > 0.6 with AE<sub>440–870 nm</sub> < 0.7 indicated desert dust type of aerosols (DDT). The remaining gaps were considered as mixed aerosol type (MXD). They reveal cases where aerosols are difficult to be discriminated bearing in mind the distinct effects of various aerosol-mixing processes in the atmosphere such as coagulation, condensation, humidification, and gas-to-particle conversion (Pace et al., 2006; Kumar et al., 2014).

### 3.2.4. Aerosol modification processes

The AE is dependent on the spectral band used for its estimation (Kumar et al., 2014). At shorter wavelengths, it provides information regarding size variation of fine-mode particles; while at longer wavelengths, it yields information about the variation in fine-to coarse-mode ratio (Kumar et al., 2015). The spectral variation of AE reflects different aerosol-type and the microphysics within the aerosol (Kaskaoutis et al., 2007; Tiwari et al., 2016). The aerosol modification processes over Mbita were examined using the graphical scheme proposed by Gobbi et al. (2007) and utilized by several authors (Kaskaoutis et al., 2011; Yu et al., 2016b; Kang et al., 2016b; Patel et al., 2017b). The method relies on the combined analysis of AE<sub>440–870 nm</sub> and its spectral curvature represented by dAE = AE<sub>440–675 nm</sub> – AE<sub>675–870 nm</sub> with fine-mode radii (R<sub>f</sub>) and FMF (η) as grid parameters in a grouped AOD. The graphical framework has been drawn using Mie theory for a typical refractive index of air m = 1.4–0.001i. More details concerning the scheme and sensitivity analysis are discussed by Gobbi et al. (2007).

The change in AE (dAE) pairs with increasing AOD<sub>675 nm</sub> provides crucial information regarding aerosol-modification processes in the atmosphere (i.e., cloud contamination, hydration, and coagulation) (Patel et al., 2017b). Negative values of dAE are associated with

negative curvature (i.e., larger values of AE indicate dominance of fine-mode particles). Positive values are associated with positive curvature (i.e., smaller values of AE suggesting dominance of coarse-mode particles associated with bimodal size distribution). A zero value of dAE represents absence of AE spectral variability (Kaskaoutis et al., 2011). Therefore, in order to investigate spectral variation of AE, its difference (dAE) at shorter (AE = 440–675 nm) and longer (AE = 675–870 nm) wavelength are calculated and plotted against  $AE_{440-870\text{ nm}}$  as a function of  $AOD_{675\text{ nm}}$ . The aerosol modification processes over Mbita were examined using daily averaged observations of AE and AODs, with the latter (at 675 nm) represented by different colors and symbol size of increasing turbidity.

## 4. Results and discussion

### 4.1. Temporal variability of aerosol properties

The daily averaged values of  $AOD_{500\text{ nm}}$ ,  $AE_{440-870\text{ nm}}$ ,  $FMF_{500\text{ nm}}$ , and CWV (cm) were used to derive long-term (2007–2015) climatology of each of the variables over Mbita. The annual mean  $AOD_{500\text{ nm}}$  ( $0.23 \pm 0.08$ ),  $AE_{440-870\text{ nm}}$  ( $1.01 \pm 0.16$ ) and  $FMF_{500\text{ nm}}$  ( $0.60 \pm 0.07$ ) investigated in the present study were lower than those reported by a number of authors (see Table 3).  $AOD_{500\text{ nm}}$  exhibited highest value in July and lowest in May (see Table 4). On the other hand,  $AE_{440-870\text{ nm}}$  was found to be maximum (minimum) in August (March); whereas, the highest (lowest) values of  $FMF_{500\text{ nm}}$  occurred in August (May). Seasonally, high  $AOD_{500\text{ nm}}$  ( $0.35 \pm 0.04$ ) with corresponding high values of  $AE_{440-870\text{ nm}}$  ( $1.14 \pm 0.17$ ) and  $FMF_{500\text{ nm}}$  ( $0.66 \pm 0.08$ ) occurred during JJA (Table 4). Meanwhile, the scatter plot of  $AOD_{500\text{ nm}}$  versus  $AE_{440-870\text{ nm}}$  noticed increasing trends with positive correlations during JJA (see Table 5 and Fig. S2 of the Supplementary Material (SM)). This suggests a large abundance of fine-mode particles associated with biomass burning activities (de Graaf et al., 2010; Boiyo et al., 2017a). In contrast, low values of  $AOD_{500\text{ nm}}$  ( $0.16 \pm 0.05$ ),  $AE_{440-870\text{ nm}}$  ( $0.84 \pm 0.05$ ), and  $FMF_{500\text{ nm}}$  ( $0.51 \pm 0.02$ ) occurred during MAM (Table 4), with decreasing trends (Table 5) and negative correlations (Fig. S2 of SM). This indicates dominance of coarse-mode relative to fine-mode particles typically associated with sea salt and desert dust (Holben et al., 2001; Schuster, 2005). Although high precipitation contributed to reduced AOD during MAM (Fig. 1e), the prolonged local dry season created favorable conditions for emission of coarse-mode dust particles resulting in low values of  $AE_{440-870\text{ nm}}$ .

The annual mean CWV ( $2.62 \pm 0.16$  cm) followed an inverse pattern to  $AOD_{500\text{ nm}}$  and  $AE_{440-870\text{ nm}}$  exhibiting the highest value in May and lowest in January (Table 4). The CWV showed low seasonal heterogeneity being relatively high during local wet than local dry seasons. The inverse relationship characterized by low correlation between the CWV and other aerosol optical properties (Table 5; Figs. S1 and S2 of SM) is consistent with the results investigated by a number of authors (Kumar et al., 2009, 2013; Adesina et al., 2014; Kang et al., 2016b; Yu

et al., 2016b; Patel et al., 2017a). This could be attributed to the presence of fine-mode non-hygroscopic particles e.g., black carbon which does not grow hygroscopically in the presence of water vapor. Also, the atmospheric water vapor and aerosols may be located at different heights and therefore, not well mixed (Singh et al., 2004; Kumar et al., 2009; Alam et al., 2011).

### 4.2. Frequency distributions of AOD, AE and CWV

The frequency distributions of  $AOD_{500\text{ nm}}$ ,  $AE_{440-675\text{ nm}}$ , and CWV during the four seasons are shown in Fig. 2. The bin interval in the present study was set to 0.1 for  $AOD_{500\text{ nm}}$  and 0.2 for  $AE_{440-675\text{ nm}}$  and CWV; and we considered all daily averaged values of  $AOD_{500\text{ nm}}$ ,  $AE_{440-675\text{ nm}}$ , and CWV in the range 0–1, 0–2, and 1.4–3.6, respectively. The large seasonal heterogeneity in  $AOD_{500\text{ nm}}$  (Fig. 2a) is attributed to the phenomena of seasonal changes in emission sources and meteorology. Despite of this, a unimodal distribution significantly skewed towards lower values was observed in all seasons, signifying dominance of a particular aerosol type. The three seasons: MAM, SON and DJF showed the strongest mode in the bin interval 0.1–0.2 accounting for 49.88%, 47.91%, and 45.33%, respectively of the total distribution. The occurrence of the strongest mode in the second lowest bin size during the three seasons with relatively lower  $AOD_{500\text{ nm}}$  averages (Table 4) showed a generally less polluted environment. However, JJA with the highest seasonal mean (Table 4) showed the strongest mode in the bin interval 0.2–0.3 accounting for 31.22% of the total distribution. This suggests a turbid atmosphere likely attributed to increased emissions resulting from changes in anthropogenic activities and meteorological conditions (Gatebe et al., 2001; de Graaf et al., 2010; Ngaina and Muthama, 2014; Boiyo et al., 2017a, b).

Meanwhile, the  $AE_{440-870\text{ nm}}$  also demonstrated a single peak distribution (Fig. 2b) similar to investigations by Adesina et al. (2014) over South Africa. The two seasons: MAM and DJF showed the strongest mode in the bin interval 0.8–0.1 accounting for 21.88% and 28.42% of their respective distributions. JJA and SON exhibited modal AE values at 1–1.2 accounting for 21.72% and 24.90% of their respective distributions. The occurrence of strongest mode at a relatively lower size bins supported by seasonal means < 1 during DJF and MAM, implies that the coarse-mode dust particles contributed more relative to fine-mode particles. In contrast, the occurrence of strong mode at relatively higher size bins, with seasonal means > 1 (Table 4) during JJA interprets more contribution of fine-mode biomass burning relative to coarse-mode dust aerosols. The CWV showed widest unimodal seasonal heterogeneity (Fig. 2c) attributed to complex seasonal patterns of precipitation (Yang et al., 2015; Ogwang et al., 2016). The two seasons: MAM and SON peaked at bin interval of 2.6–2.8 accounting for 18.63% and 22.80%, respectively of the total distributions. On the other hand, JJA and DJF peaked at 2.8–3 accounting for 28.72% and 21.02%, respectively of the total distribution. Notably, the annual frequency distributions of  $AOD_{500\text{ nm}}$ ,  $AE_{440-675\text{ nm}}$ , and CWV were peaked at the bin intervals of 0.1–0.2, 1–1.2, and 2.6–2.8, respectively (Fig. S3 of SM),

Table 3

Comparison of aerosol optical properties (unitless) and radiative forcing (in  $W\ m^{-2}$ ) observed at different sites. The AOD values indicated with asterisk (\*) are measured at 440 nm.

Study site	Country	Environment	Period	$AOD_{500\text{ nm}}$	$AE_{440-870\text{ nm}}$	$SSA_{440\text{ nm}}$	$ARF_{ATM}$	Citation
Mbita	Kenya	Rural	2007–2015	0.23	1.01	0.89	23.77	Present study
Beijing	China	Urban	2001–2014	1.20*	0.44	0.88	116.72	Yu et al. (2016b)
Nanjing	China	Urban	2007–2008	0.95	1.10	0.91	37.0	Kang et al. (2016b)
Skukuza	South Africa	Rural	1999–2010	0.25*	1.40	–	13.96	Adesina et al. (2017)
Pretoria	South Africa	Urban	2011–2015	0.23*	1.50	0.91	19.82	Kumar et al. (2017)
Karachi	Pakistan	Coastal	2007–2013	0.48	0.60	0.90	51.64	Bibi et al. (2016)
Lahore	Pakistan	Urban	2007–2013	0.64	0.88	0.88	27.0	Bibi et al. (2016)
Kanpur	India	Urban	2007–2013	0.67	0.97	0.89	37.0	Bibi et al. (2016)
Desalpar	India	Rural	2014–2015	0.43	0.69	–	16.59	Patel et al. (2017a)
Kavaratti	India	Rural	2009–2014	0.51	1.36	–	7.94	Patel et al. (2017b)
Anantapur	India	Semi-arid	2013–2014	0.35	1.09	0.81	25.05	Kalluri et al. (2016)

**Table 4**

The monthly, seasonal, and annual variations of different aerosol optical and radiative parameters measured at Mbita during the entire study period. All the parameters are unitless except, CWV and ARF defined in terms of 'cm' and 'W m<sup>-2</sup>', respectively.

Month	AOD <sub>500 nm</sub>	CWV	AE <sub>440–870 nm</sub>	FMF <sub>500 nm</sub>	SSA <sub>440 nm</sub>	ASY <sub>440 nm</sub>	ARF <sub>ATM</sub>
January	0.23 ± 0.07	2.33 ± 0.31	1.03 ± 0.15	0.60 ± 0.04	0.88 ± 0.01	0.72 ± 0.01	28.35 ± 17.26
February	0.28 ± 0.11	2.41 ± 0.40	0.85 ± 0.13	0.53 ± 0.09	0.88 ± 0.04	0.70 ± 0.01	22.31 ± 8.00
March	0.22 ± 0.06	2.44 ± 0.17	0.80 ± 0.12	0.53 ± 0.03	–	0.71 ± 0.01	2.09 ± 47.88
April	0.14 ± 0.02	2.75 ± 0.18	0.83 ± 0.14	0.50 ± 0.08	–	0.73 ± 0.04	3.16 ± 34.22
May	0.14 ± 0.05	2.85 ± 0.18	0.89 ± 0.27	0.50 ± 0.09	–	0.70 ± 0.03	18.1 ± 19.58
June	0.35 ± 0.13	2.76 ± 0.13	0.94 ± 0.21	0.57 ± 0.14	0.91 ± 0.06	0.71 ± 0.02	28.79 ± 12.91
July	0.38 ± 0.07	2.56 ± 0.12	1.21 ± 0.21	0.68 ± 0.11	0.90 ± 0.04	0.71 ± 0.01	36.69 ± 13.46
August	0.30 ± 0.05	2.68 ± 0.13	1.26 ± 0.15	0.72 ± 0.10	0.90 ± 0.03	0.71 ± 0.01	35.51 ± 8.74
September	0.23 ± 0.04	2.66 ± 0.05	1.21 ± 0.13	0.67 ± 0.07	–	0.71 ± 0.02	33.3 ± 24.30
October	0.18 ± 0.05	2.69 ± 0.14	1.06 ± 0.17	0.60 ± 0.09	–	0.71 ± 0.02	29.37 ± 10.60
November	0.15 ± 0.02	2.72 ± 0.20	1.05 ± 0.11	0.62 ± 0.07	–	0.71 ± 0.01	21.28 ± 12.28
December	0.17 ± 0.06	2.56 ± 0.21	1.03 ± 0.12	0.62 ± 0.06	0.89 ± 0.02	0.72 ± 0.03	26.31 ± 11.86
MAM	0.16 ± 0.05	2.68 ± .21	0.84 ± 0.05	0.51 ± 0.02	–	0.71 ± 0.01	7.78 ± 8.95
JJA	0.35 ± 0.04	2.66 ± 0.10	1.14 ± 0.17	0.66 ± 0.08	0.90 ± 0.01	0.71 ± 0.03	33.66 ± 4.26
SON	0.19 ± 0.04	2.69 ± 0.03	1.11 ± 0.09	0.63 ± 0.04	–	0.71 ± 0.02	27.98 ± 6.12
DJF	0.23 ± 0.06	2.44 ± 0.12	0.97 ± 0.10	0.58 ± 0.04	0.88 ± 0.00	0.71 ± 0.03	25.66 ± 3.07
Annual	0.23 ± 0.08	2.62 ± 0.12	1.01 ± 0.14	0.60 ± 0.07	0.84 ± 0.07	0.71 ± 0.03	23.77 ± 11.18

**Table 5**

Seasonal and annual statistics for the evaluation of relationship between the aerosol optical properties measured at Mbita during the study period. It includes the slope and intercept of the linear regression fitting, correlation coefficient (r) and the number (N) of data points in both datasets. The value next to mean corresponds to the standard deviation. The representation of scatter plots in the figures is given as Figs. S1 and S2 of SM.

Relationship	Season	Intercept	Slope	r	N
AOD vs AE	MAM	1.09 ± 0.03	−1.65 ± 0.15	−0.48	425
	JJA	1.06 ± 0.03	0.21 ± 0.09	0.10	571
	SON	1.13 ± 0.04	−0.19 ± 0.17	−0.05	478
	DJF	0.92 ± 0.03	0.20 ± 0.09	0.12	367
	Annual	0.96 ± 0.01	0.23 ± 0.05	0.10	1841
AE vs CWV	MAM	0.40 ± 0.09	0.15 ± 0.03	0.21	425
	JJA	0.76 ± 0.13	0.14 ± 0.05	0.12	571
	SON	0.83 ± 0.12	0.10 ± 0.05	0.10	478
	DJF	0.40 ± 0.09	0.15 ± 0.03	0.21	367
	Annual	0.62 ± 0.05	0.15 ± 0.02	0.17	1841
AOD vs CWV	MAM	2.82 ± 0.04	−0.98 ± 0.22	−0.21	425
	JJA	2.54 ± 0.03	0.29 ± 0.07	0.17	571
	SON	2.60 ± 0.04	0.49 ± 0.17	0.13	478
	DJF	2.31 ± 0.04	0.51 ± 0.14	0.19	367
	Annual	2.58 ± 0.02	0.16 ± 0.06	0.06	1841

and followed a relatively similar pattern as the seasonal frequency distribution.

#### 4.3. Spectral characteristics of AOD

The spectral AOD is a key parameter in estimating the extent to which aerosols directly influence the radiative balance of the earth-atmosphere system (Kaskaoutis et al., 2009). It is dependent on the columnar abundance, size distribution and refractive index of aerosols. Fig. 3a features a contour plot representing measured AOD at 7 wavelengths (340, 380, 440, 500, 675, 870, and 1020 nm) observed at Mbita during the entire study period. The monthly and seasonal spectral variations averaged over all the years during the study period are shown in Fig. 3b and c, respectively. The observed decrease in AOD with increasing wavelength in all panels indicates systematic spectral dependence following the classical Mie scattering theory. AOD values at shorter wavelengths were greater than 0.18 compared to values of ~0.14 at a longer wavelength. High AOD values at shorter wavelengths are associated with dominance of fine-mode aerosols; whereas, low AODs at longer wavelengths shows abundance of coarse-mode aerosols. The presence of higher concentration of fine-mode particles which are selective scatterers enhances irradiance scattering, resulting in high AOD at shorter wavelengths (Kumar et al., 2009, 2014; Patel et al., 2017a).

The spectral AOD is relatively higher in 2011 followed by 2013 indicating high aerosol loading during the two years. Meanwhile, monthly and seasonal spectral AOD (Fig. 3b and c) show relatively lower spectral dependence during MAM and SON due to higher amounts of coarse-mode dust particles. In contrast, the high spectral gradient during JJA and DJF confirms the presence of fine-mode particles, being enhanced during the latter season. As expected, maximum AODs at different spectral wavelengths occurred during the local dry seasons, while minimum ones were characterized during the wet seasons. This is consistent with AOD distribution over EA and is attributed to changes in climatic conditions, emission sources, and anthropogenic activities (Ngaina and Muthama, 2014; Boiyo et al., 2017a,b).

#### 4.4. Curvature effect on AOD and AE

In order to get further information regarding the nature of aerosol size distribution discussed in Section 3.2.1, the coefficients  $a_1$  and  $a_2$  obtained through application of the second-order polynomial fit in the spectral range 340–870 nm were analyzed as a function of AOD<sub>500 nm</sub> and AE<sub>440–870 nm</sub> for all the seasons (Fig. 4). The seasonal cycle of  $a_1$  is dominated by negative values being generally higher ( $< -1.0$ ) for large ( $> 1.0$ ) values of AE<sub>440–870 nm</sub> (Fig. 4a and e). Highest negative values of  $a_1$  ( $< -1.0$ ) with corresponding high values of AOD<sub>500 nm</sub> ( $> 0.3$ ) and AE<sub>440–870 nm</sub> ( $> 1.0$ ) occurred during JJA (Fig. 4a and e). This indicates dominance of fine-mode aerosols resulting from biomass burning. As evidenced in Fig. 4b, low AOD<sub>500 nm</sub> ( $< 0.3$ ) is associated with wide variability in  $a_2$  of both positive and negative curvatures. In contrast, for higher AOD<sub>500 nm</sub> values,  $a_2$  tends to zero or negative indicating negative curvature. High negative values in  $a_2$  occur during JJA followed by DJF (Fig. 4b). This shows abundance of fine-mode particles due to enhanced biomass burning activities (both seasons), and due to photochemical process resulting from intense solar radiation during DJF. On the other hand, significant number of data points shows positive values of  $a_2$  during MAM and SON likely due to dust particles resulting from prolonged dry seasons. Large negative values of  $a_2$  identified with  $\alpha > 1.0$  supports the presence of fine-mode biomass burning aerosols, whereas positive values for  $\alpha < 1.0$  indicates abundance of coarse-mode dust and sea-salt aerosols (Fig. 4f).

Previous studies indicated that for the same wavelength,  $a_2 - a_1 = \alpha$  (Kaskaoutis et al., 2007; Kedia et al., 2014). In order to verify this claim, the  $a_2 - a_1$  versus  $\alpha_{440–870}$  was plotted (Fig. 4g). It is revealed that majority of data points were scattered around the line  $y = x$  with high correlation of 0.96. This depicts high accuracy in the retrievals of the spectral AOD and  $\alpha$ , implying that the  $a_2 - a_1$  versus AOD<sub>500 nm</sub> scatter plot shown in Fig. 4c is similar to Fig. 5. Values of

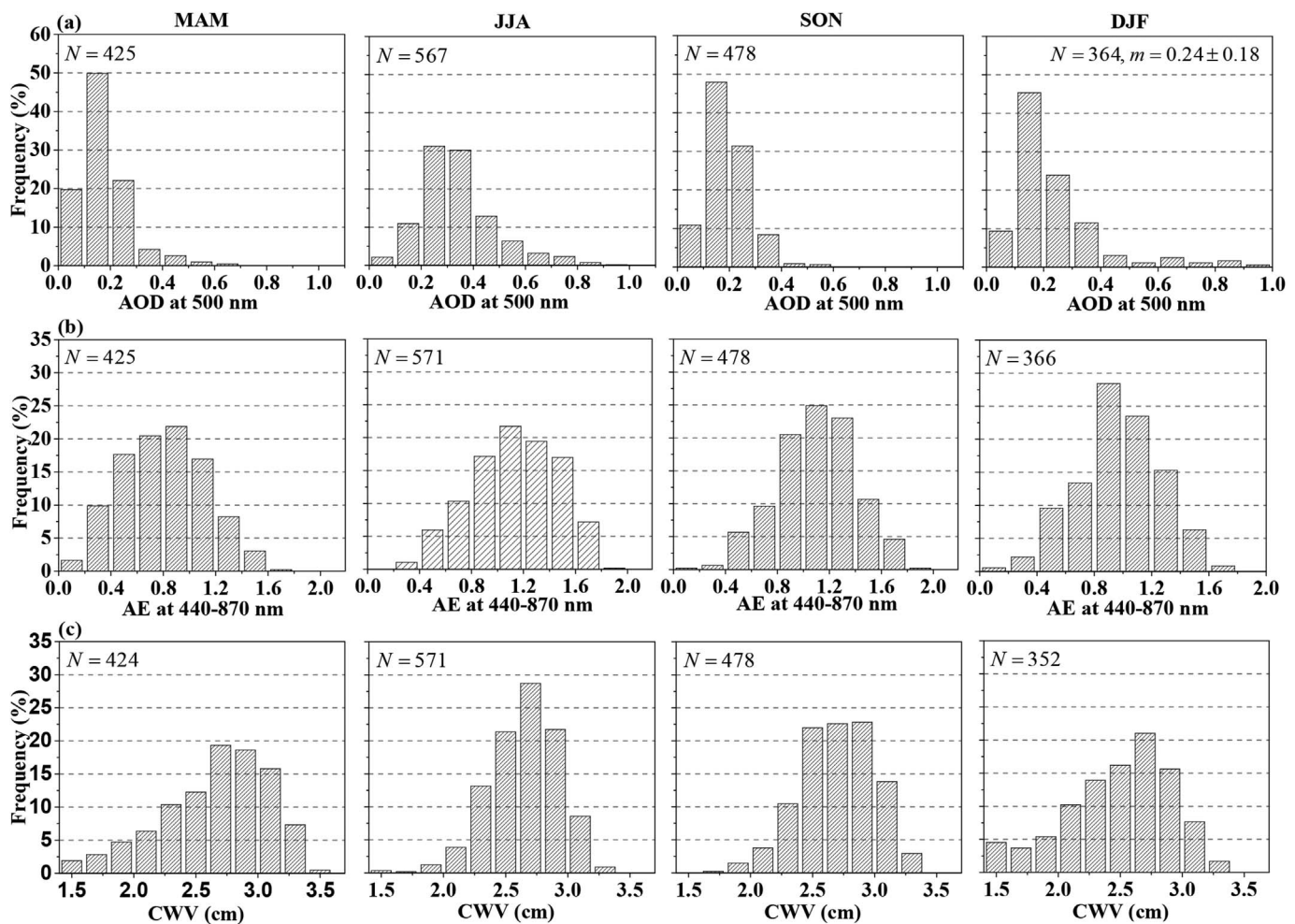


Fig. 2. Seasonal frequency distributions (%) of (a) AOD<sub>500 nm</sub>, (b) AE<sub>440–870 nm</sub> and (c) CWV. N corresponds to the number of observed days over Mbita during 2007–2015.

$a_2 - a_1 \geq 2$  ( $a_2 - a_1 \leq 1$ ) represent AOD spectra dominated by fine (coarse)-mode aerosols, whereas  $1 < a_2 - a_1 < 2$  represent a wide range of fine-mode fractions and/or mixture of modes (Kedia et al., 2014). In the present study,  $a_2 - a_1$  in the range 0.14–1.63 revealed a mixture of modes.

Fig. 4d shows the scatter plot between AOD<sub>500 nm</sub> and  $\alpha'$  for each season. Majority of  $\alpha'$  were positive for a wide range of AOD<sub>500 nm</sub> and high AE<sub>440–870 nm</sub> (Fig. 4h) suggest increased contribution of fine-mode particles. However, near-zero or negative values of  $\alpha'$  indicate contribution of coarse-mode relative to fine-mode particles (Reid et al., 1999; O'Neill et al., 2001). For small AOD<sub>500 nm</sub>, there are a large ranges of values both negative and positive (from  $-1.5$  to  $+2.5$ ). This is an indication of bimodal aerosol size distribution at relatively lower AODs, with dominance of fine- and coarse-mode particles (Eck et al., 1999). Notably, since  $\alpha' = -2a_2$ , the findings extracted from Fig. 4d and h are same as those in Fig. 4b and f, respectively. A similar relationship for AOD versus  $\alpha'$  has recently been observed by several authors (e.g., Kumar et al., 2013; Kang et al., 2016b; Kalluri et al., 2016; Patel et al., 2017a) over different environments. It can, therefore, be concluded that Mbita and its environments are generally characterized by fine-mode aerosols produced from biomass burning during JJA and DJF. Hence, there is a tendency towards large positive values of  $\alpha'$  especially as AOD values increases due to strong optical influence of fine-mode particles at higher AOD. The large negative values for very small AODs indicate significant departure from linearity (Eq. (3)) under a clean atmosphere. This is consistent with previous investigations (Kaskaoutis and Kambezidis, 2006; Kedia et al., 2014; Kumar et al., 2013; Kalluri et al., 2016; Patel et al., 2017a) over different environments.

#### 4.5. Aerosol type classification and their contributions

A close examination of the contour density plots between AOD<sub>500 nm</sub> and AE<sub>440–870 nm</sub> reveals areas of maximum density representing different aerosol types for different seasons over Mbita (Fig. 5). During MAM, the maximum density area was observed for the pair (AOD<sub>500 nm</sub>, AE<sub>440–870 nm</sub>) = (0.1, 0.9), indicating low turbid conditions likely influenced by mixed aerosol field with a larger fraction of coarse-mode particles. During JJA, the MAM maximum shifts into three; one with AOD<sub>500 nm</sub> = 0.3 and AE<sub>440–870 nm</sub> = 0.6 representing turbid condition influenced by coarse-mode dust particles and second with AOD<sub>500 nm</sub> = 0.3–0.4 and AE<sub>440–870 nm</sub> = 0.8–1.0 indicating turbid conditions under MXD aerosols type, with predominance of coarse-mode particles. The third correspond to AOD<sub>500 nm</sub> = 0.4 and AE<sub>440–870 nm</sub> = 1.2 indicating high turbid conditions due to fine-mode biomass burning or urban-industrial (BUI) type of aerosols. The widest maximum density area (AOD<sub>500 nm</sub> = 0.1–0.2, AE<sub>440–870 nm</sub> = 0.9–1.3) during SON indicates a relatively low turbid conditions likely under influence of CCB, with a mixture of coarse- and fine-mode particles. During DJF, the maximum density area located at AOD<sub>500 nm</sub> = 0.1–0.3, AE<sub>440–870 nm</sub> = 0.8–1.0 shows a moderate turbid conditions, with mixed aerosol fields dominated by coarse-mode particles.

The percentage contribution of each of the four different aerosol types over Mbita based on the AOD<sub>500 nm</sub> and AE<sub>440–870 nm</sub> threshold values are represented by the numerals enclosed within the parenthesis in all panels of Fig. 5, while the corresponding fractional pies are shown in Fig. S5 of SM. The MXD aerosol type was found to be predominant in all seasons, being more pronounced during JJA (32.81%). Further, the



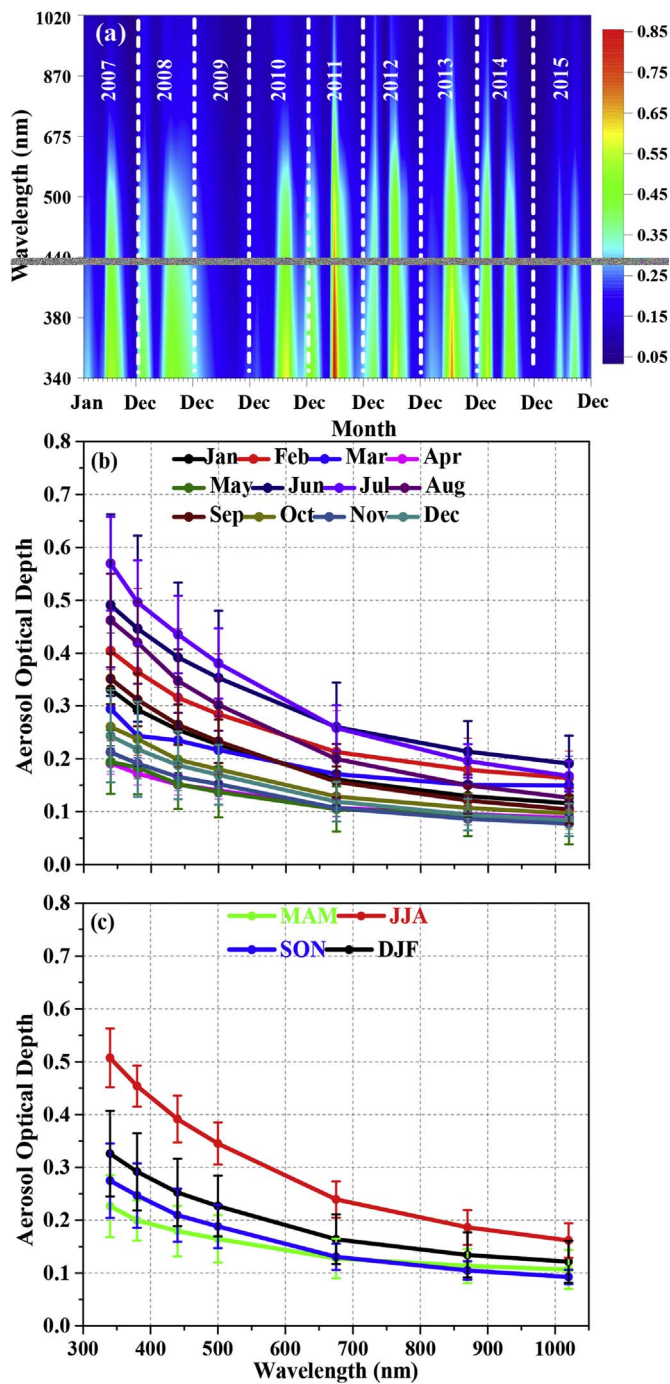


Fig. 3. (a) Contour plot representing the spectral characteristics of monthly mean AOD for all the years during the entire study period. The months with very low ( $< 0.05$ ) or missing spectral AOD in Fig. 3a are indicated by deep blue color. (b) Monthly and (c) seasonal spectral characteristics of AOD observed at Mbata during the study period. The vertical lines through the points in panels (b) and (c) correspond to the standard deviation of the mean. (For interpretation of the references to color in this figure legend, the reader is referred to the Web version of this article.)

CMA and CCB aerosol types exhibited their highest relative contribution of 50.82% and 52.72% during MAM and SON, respectively. On the other hand, 37.72%, 32.81%, and 1.40% of BUI, MXD and DDT, respectively were observed during JJA. The low contribution of DDT in all seasons is due to large proximity from the dust zones. Also the enhanced precipitation over the site (Fig. 1e) caused large wet deposition of aerosols and prevented their surface emission. Since the majority of aerosols dominated during JJA, more mitigations measures should

focus on this season towards ensuring a relatively clean environment.

#### 4.5.1. Aerosol types from AAE vs EAE

Knowledge of aerosol spectral absorption is used to determine dominance of dust, carbonaceous matter, or hygroscopic aerosols (e.g., sulfates, nitrates, or sea salt). Notably, the extinction Ångström exponent (EAE) could be used as an indicator of the dominance of carbonaceous aerosols (e.g., Black Carbon; BC and Organic Carbon; OC) or iron oxides in the dust; whereas, the absorption Ångström exponent (AAE) indicates the magnitude of their absorption. However, these parameters alone cannot fully describe the dominant aerosol type. In the present work, a combination EAE and AAE parameters were further used to categorize the dominant aerosol type from the AERONET retrievals. With  $AAE_{440-870 \text{ nm}}$  and  $EAE_{440-870 \text{ nm}}$  values in the ranges 0.79–1.11 and 0.36–1.30, respectively, the threshold values for constructing the scatter diagram (Fig. 6a) were slightly altered from those previously utilized by a number of authors (Russell et al., 2009; Giles et al., 2012; Che et al., 2015; Yu et al., 2016b; Patel et al., 2017a). Biomass burning (BB) which was characterized by  $EAE > 1.2$  with  $AAE > 1.0$ , constituted the dominant aerosol type over Mbata, with percentage contribution of 60.59%. This is attributed to increased smoke plumes from nearby agricultural crop-residue burning. Cases corresponding to the turbid atmosphere resulting from urban/industrial (UI) plumes were represented by  $EAE > 1.2$  and  $AAE < 1.0$ . The UI hold significant fraction (12.37%) due to its proximity ( $\sim 100 \text{ km}$ ) to Kisumu city. Furthermore, DDT represented by  $EAE < 0.7$  and  $AAE > 1.5$ , was observed the least (1.19%) due to large proximity of the site to dust source regions. The MXD category made significant contribution 25.89% during the entire study period.

#### 4.6. Modification of aerosols

The aerosol modification processes are depicted using a graphical scheme based on Gobbi et al. (2007) to study for annual (Fig. S6) and seasonal characteristics (Fig. 7). Regarding  $AOD_{675 \text{ nm}} < 0.2$  ( $> 0.3$ ) as low (high) values over Mbata, some key features are obvious from the annual scatter plot of  $AE_{440-675 \text{ nm}}$  versus  $dAE$ . A large variation in  $AE_{440-675 \text{ nm}}$  versus  $dAE_{\text{nm}}$  was observed, suggesting significant heterogeneity in the dominant particle sizes with a mixture of fine- and coarse-mode particles. Low values of  $AOD_{675 \text{ nm}}$  found outside the classification scheme are attributed to large errors in estimation of  $AE_{440-675 \text{ nm}}$  and  $dAE$ , as well as uncertainties while measuring  $AOD_{675 \text{ nm}}$  (Kaskaoutis et al., 2011; Kang et al., 2016b). Two sets of high  $AOD_{675 \text{ nm}}$  are evident (Fig. S6). The first set, which is associated with high  $AE_{440-675 \text{ nm}}$  (1.2–1.8),  $\eta > 70\%$ ,  $dAE < 0$  and  $R_f \sim 0.10$ –0.17, indicates addition of fine-mode particles (i.e., anthropogenic pollution and/or biomass burning). The increase in  $R_f$  ( $\sim 0.10$ –0.17) for these data points indicates that turbid condition over Mbata are linked to hygroscopic growth and/or coagulation from aging of the fine-mode aerosols leading to larger values of  $R_f$  (0.10–0.2) and  $\eta$  ( $> 70\%$ ). The second set of high  $AOD_{675 \text{ nm}}$  exhibits low  $AE_{440-870 \text{ nm}}$  ( $< 1.0$ ),  $\eta < 50\%$  or even  $< 30\%$ ,  $dAE > 0$  and  $R_f \sim > 0.17$ , suggesting predominance of coarse-mode particles likely due to the impact of dust aerosols.

The seasonal scatter plots of  $AE_{440-870 \text{ nm}}$  and  $dAE$  exhibits unmistakable differences regarding the presumed aerosol modification processes during the four different climatic seasons over Mbata (Fig. 7a–d). A majority of data points with high AOD during MAM and SON were found in the coarse-mode growth wing ( $dAE > 0$ ,  $\eta < 30\%$ ), being more pronounced in the former season. This could be attributed to dust particles occasioned by prolonged dry season. The presence of large number of data points with high  $AE_{440-675 \text{ nm}}$  ( $> 1.2$ ),  $\eta > 70\%$  and very low values of  $dAE$  ( $< 0$ ) during JJA interprets predominance of fine-mode particles, likely due to biomass burning activities and urban-industrial aerosols (de Graaf et al., 2010; Makokha and Angeyo, 2013). A few cases with high AODs, low  $\eta$  ( $< 30\%$ ) and  $dAE > 0$

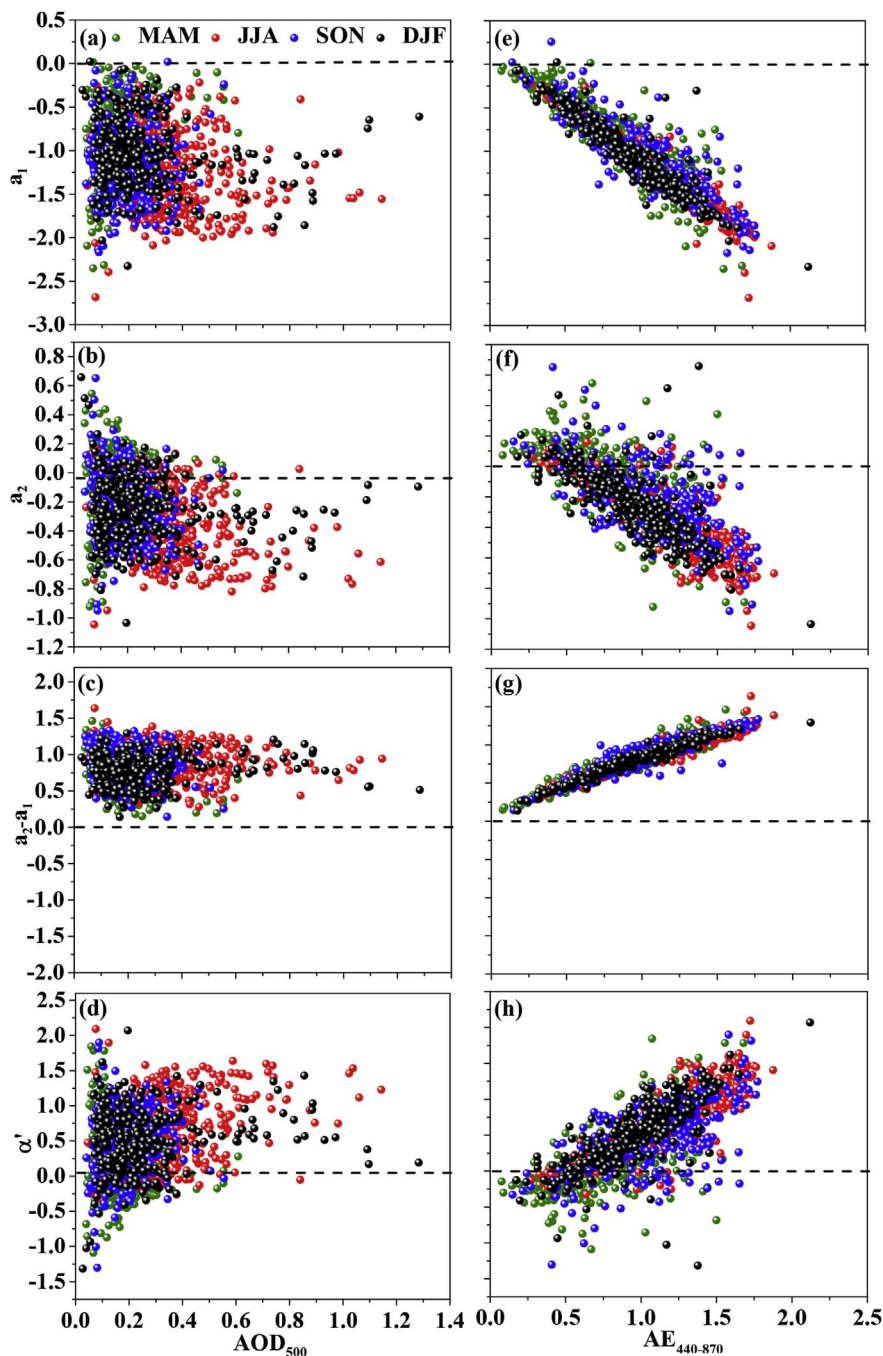


Fig. 4. Scatter plot between  $a_1$ ,  $a_2$ , differences of polynomial coefficients  $a_1$  and  $a_2$  ( $a_2 - a_1$ ) and derivative of AE ( $\alpha'$ ) versus  $AOD_{500\text{ nm}}$  (a–d) and  $AE_{440-870\text{ nm}}$  (e–h) for the study period observed at Mbita.

scattered in the coarse-mode growth wing ( $\eta < 30\%$  and  $dAE > 0$ ) during this season are likely due to impact of dust aerosols. High AODs during DJF shows a shift to smaller AE values ( $< 0.8$ ), positive dAE values with  $\eta$  values  $< 30\%$ , suggesting predominance of coarse-mode dust particles resulting from change in emission sources (Boiyo et al., 2017a,b). It can therefore be inferred that high AODs at Mbita may be associated with increased concentration of fine- and coarse-mode particles. The fine-mode particles dominate during JJA, while the coarse-mode particles are observed during JJA and DJF, with limited contribution during MAM.

#### 4.7. Aerosol microphysical properties and optical spectral dependencies

##### 4.7.1. Aerosol volume size distribution

Fig. 8 shows the monthly and seasonal evolution of the aerosol

volume size distribution (VSD) retrieved from the Sun photometer using 22 bin radii in the size range of  $0.05\text{--}15\text{ }\mu\text{m}$ . The size distribution reveals two distinct modes: fine (particle size  $< 0.6\text{ }\mu\text{m}$ ) and coarse (particle size  $> 0.6\text{ }\mu\text{m}$ ), similar to the observations made by a number of authors (Dubovik et al., 2002; Singh et al., 2004; Alam et al., 2011, 2012; Adesina et al., 2014, 2017; Yu et al., 2016b; Patel et al., 2017a; Kumar et al., 2017) over different environments. The fine-mode (with radius of about  $0.15\text{ }\mu\text{m}$ ) showed highest values in July and lowest in April, with volume concentrations of  $0.049$  and  $0.0097\text{ }\mu\text{m}^3\text{ }\mu\text{m}^{-2}$ , respectively (Fig. 8a). On the other hand, the coarse-mode with radius of about  $5.06\text{ }\mu\text{m}$  ( $3.86\text{ }\mu\text{m}$ ) has highest (lowest) value in July (May) and volume concentration of  $0.0692$  ( $0.0196\text{ }\mu\text{m}^3\text{ }\mu\text{m}^{-2}$ ). The seasonally averaged VSD over Mbita showed significant seasonal heterogeneity in volume concentration with more or less similar peak radii of  $0.15$  and  $5.06\text{ }\mu\text{m}$  for fine- and coarse-mode particles, respectively (Fig. 8b). A

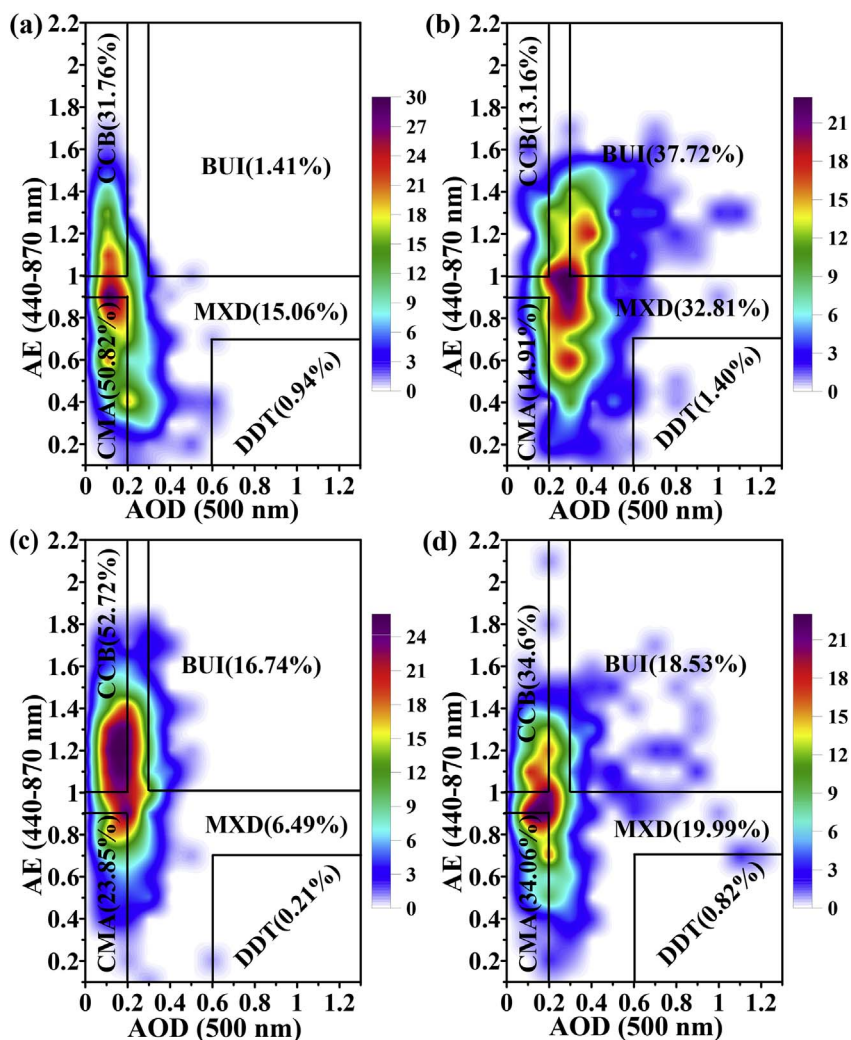


Fig. 5. Contour density plots between  $AOD_{500\text{ nm}}$  and  $AE_{440-870\text{ nm}}$  for different seasons (a) MAM (b) JJA (c) SON (d) DJF indicating major aerosol types over Mbita. The numerals enclosed in brackets in each panel represent fractional contribution of each aerosol type to the total in each season during the study period, while the corresponding fractional pies are shown in Fig. S5 of SM. The black solid boxes in all the panels represent threshold values for each aerosol type. CMA–Clean Marine type; CCB–Continental Clean Background type; BUI– Biomass burning/Urban-Industrial type; DDT–Desert dust type; and MXD–Mixed type aerosols. The colored scale indicates the density of data points.

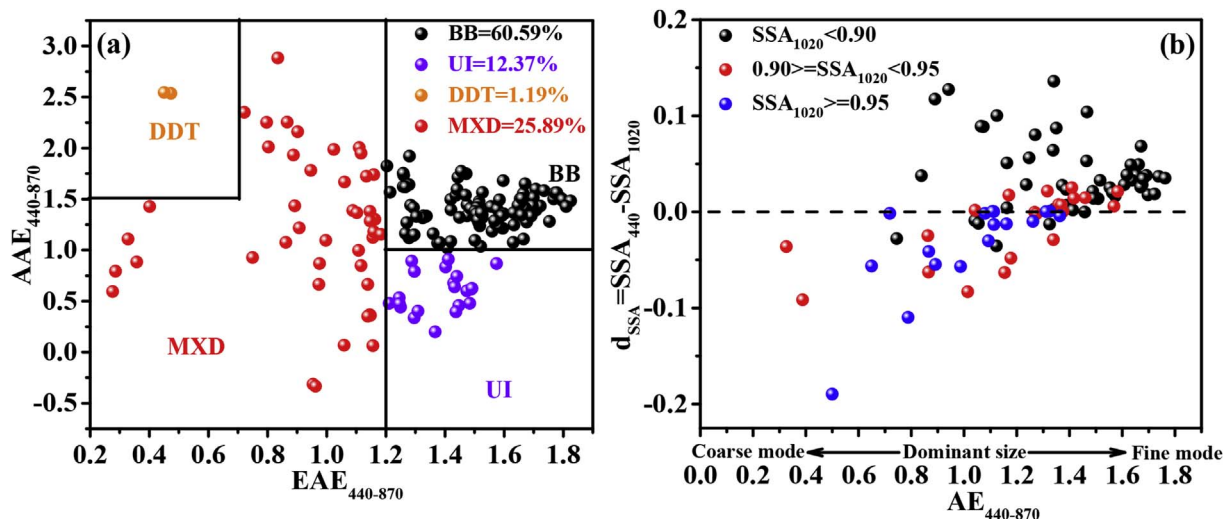


Fig. 6. Scatter plot of  $EAE_{440-870\text{ nm}}$  versus  $AAE_{440-870\text{ nm}}$  for identifying dominant aerosol types during the study period. The percentage contribution of each aerosol type is also shown in all the panels. (b) Difference of SSA ( $d_{SSA} = SSA_{440\text{ nm}} - SSA_{1020\text{ nm}}$ ) versus  $AE_{440-870\text{ nm}}$  for different ranges of  $SSA_{1020\text{ nm}}$  over Mbita during the study period.

prominently high volume concentration in fine-mode is evident during JJA ( $\sim 0.047\text{ }\mu\text{m}^3\text{ }\mu\text{m}^{-2}$ ) being approximately twice that of DJF and SON and fourth that of MAM. This suggests strong loading of anthropogenic aerosols resulting from frequent biomass burning activities which are more pronounced in July and August (Fig. 8a). This coincides

with highest values of  $AOD_{500\text{ nm}}$ ,  $AE_{440-870\text{ nm}}$  and  $FMF_{500\text{ nm}}$  (Table 4). The highest volume concentration in the coarse-mode was also noticed during JJA ( $0.0546\text{ }\mu\text{m}^3\text{ }\mu\text{m}^{-2}$ ), followed by MAM ( $\sim 0.047\text{ }\mu\text{m}^3\text{ }\mu\text{m}^{-2}$ ) and lower during SON ( $0.091\text{ }\mu\text{m}^3\text{ }\mu\text{m}^{-2}$ ). The presence of coarse-mode particles during MAM, despite of heavy



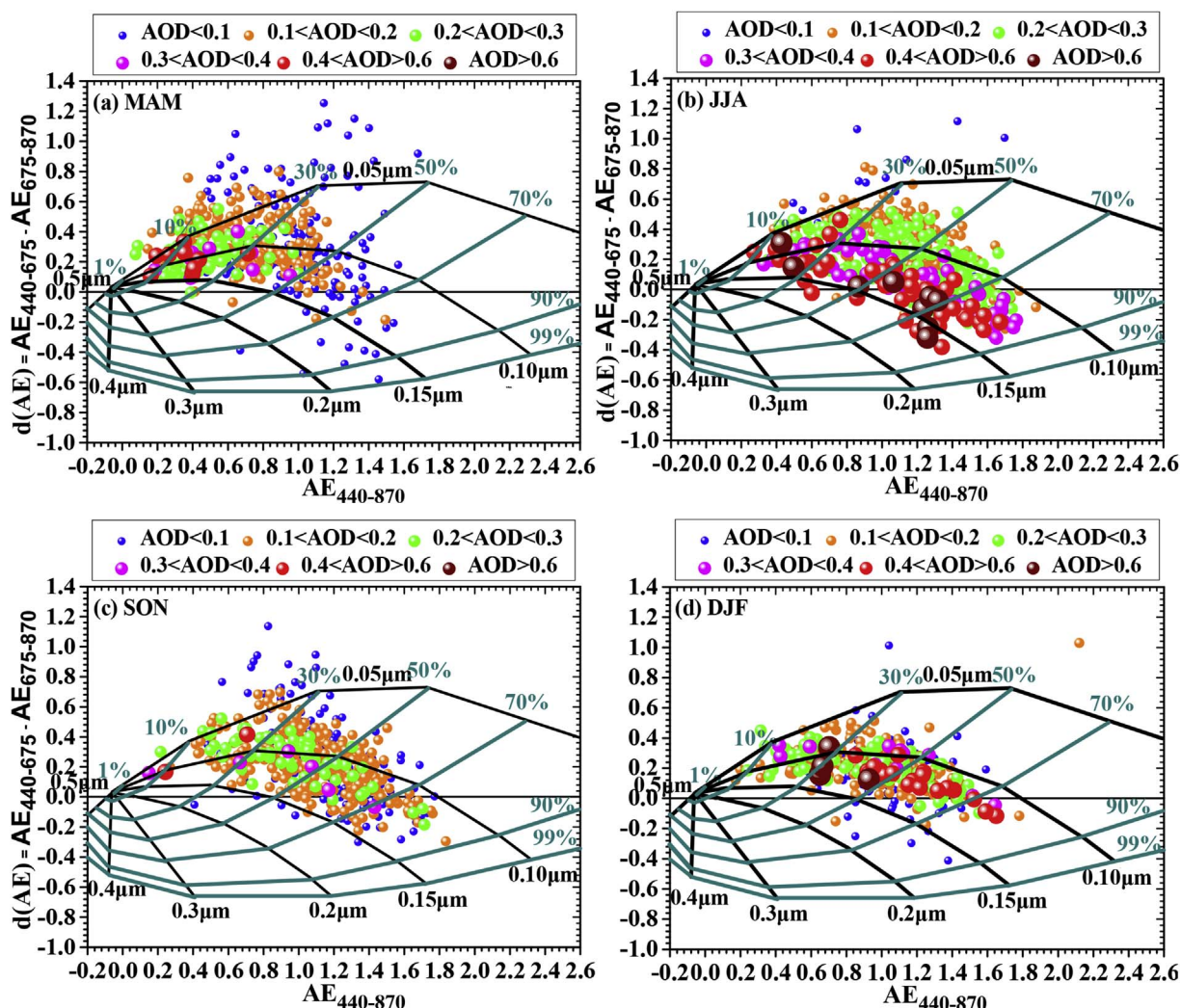


Fig. 7. Ångström exponent difference,  $dAE = AE(440-675 \text{ nm}) - AE(675-870 \text{ nm})$  as a function of  $AE(440-870 \text{ nm})$  and  $AOD_{675 \text{ nm}}$  (color-sized scale) over Mbita during four seasons for bimodal and log-normal size distributions. The different colors of closed circles represent values of  $AOD_{675 \text{ nm}}$  with increasing turbidity represented by the size of the circle. The black solid and dark cyan lines are for the fixed size of fine-mode effective radius ( $R_f$ ) and fixed fractional contribution of fine-mode to AOD at 675 nm ( $\eta$ ), respectively. (For interpretation of the references to color in this figure legend, the reader is referred to the Web version of this article.)

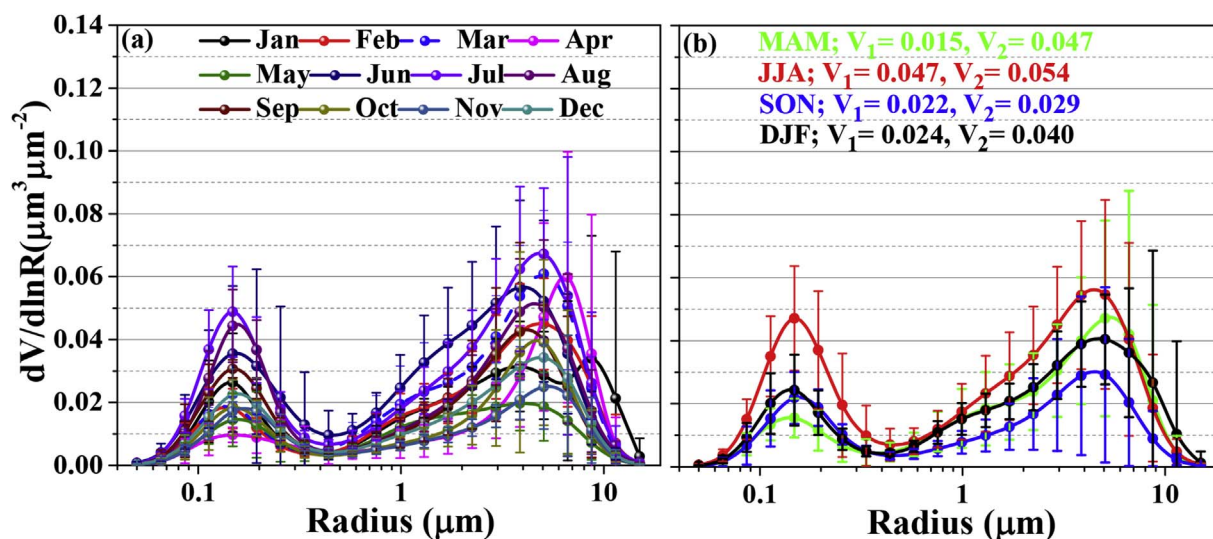


Fig. 8. Aerosol volume size distribution observed at Mbita in different (a) months, (b) seasons during the study period along with the standard deviations.  $V_1$  and  $V_2$  represent volume concentration ( $\mu\text{m}^3 \mu\text{m}^{-2}$ ) for fine- and coarse-modes, respectively. The geometric mean radii of fine and coarse modes are observed at 0.15 and 5.06  $\mu\text{m}$ , respectively during all seasons.



precipitation, could be associated with dust particles resulting from the prolonged dry season (de Graaf et al., 2010; Makokha and Angeyo, 2013). Therefore, high AOD during JJA is attributed to a combination of fine- and coarse-mode particles.

#### 4.7.2. Spectral dependencies of SSA

The direct effect of scattering and absorbing particles in terms of cooling or warming of the atmosphere depends on the single scattering albedo (SSA), defined as the ratio of the scattering to extinction (scattering + absorption). SSA relates the fraction of radiation absorbed by the atmosphere (1-SSA) and is a key parameter in assessing ARF (Singh et al., 2004). The spectral variation of SSA gives useful information regarding dominance of a particular aerosol type (Alam et al., 2012; Patel et al., 2017a). The annual mean  $SSA_{440\text{ nm}}$  ( $0.89 \pm 0.03$ ) ranged from  $0.88 \pm 0.01$  to  $0.91 \pm 0.06$  (Table 4) close to those examined by Patel et al. (2017a) over Desalpar but less than those found in other regions (Table 3). Such disparity is attributed to differences in meteorological conditions, geographical locations, and prevailing aerosol types (Alam et al., 2012). SSA showed a distinct spectral variation, implying significant changes in the dominant aerosol type (Fig. 9a). It decreased with increasing wavelength in July and August due to fine-mode absorbing aerosols (mostly BUI) over coarse-mode scattering particles (Singh et al., 2004; Yu et al., 2016b). Lower values of SSA were observed at higher wavelengths. This is because interaction of aerosols with incoming solar radiation is minimum at longer wavelength (Kang et al., 2016b). On the other hand, SSA increased with wavelengths in February indicating predominance of coarse-mode scattering aerosols (mainly dust) over absorbing particles (Alam et al., 2011; Cheng et al., 2015; Yu et al., 2016b; Bibi et al., 2016; Iftikhar

et al., 2017). In December, January and June, SSA significantly increased at shorter wavelengths (440–670 nm) followed by a decrease at longer wavelengths (670–1020 nm) attributed to mixing of dust with the anthropogenic aerosols. Overall, SSA increased with wavelength during DJF due to presence of highly scattering dust particles from visible to the near-infrared spectrum. In contrast, SSA decreased with increasing wavelength during JJA due to dominance of absorbing biomass burning aerosols over the site. SSA is one of the key parameters in determining the effect of aerosol particles on the climate. Singh et al. (2004) suggested that the effect of aerosol could shift from cooling to warming if SSA goes below a critical value (0.86). The SSA investigated in the present study is above this critical value (Table 4) suggesting a possible local cooling effect in the BOA.

In order to assess the absorbing aerosols and associate their absorbing capacity versus the aerosol particle-size, the present study further analyzed the difference between SSA at 440 nm and 1020 nm ( $d_{SSA}$ ) and correlated with  $AE_{440-870}$  at three levels of  $SSA_{1020\text{ nm}}$  (Fig. 6b). Negative values of  $d_{SSA}$  indicates absorption of iron oxide at 440 nm mainly found in dust, whereas positive ones demonstrate absorption by BC particles at 1020 nm (Derimian et al., 2008; Dumka et al., 2014). It is evident (Fig. 6b) that as  $AE_{440-870}$  increases from low (0.33) to high (1.76) values, indicating decreasing (increasing) contribution of coarse (fine)-mode particles, the spectral SSA changes from strong absorption at 440 nm (negative  $d_{SSA}$ ) to another strong absorption at 1020 nm (positive  $d_{SSA}$ ). The present study selected  $AE_{440-870} = 0.8$  as the threshold between coarse- and fine-mode. For fine-mode particles, the absorption at 440 nm is limited since  $SSA_{1020\text{ nm}} < 0.90$  dominate the zone  $AE_{440-870} > 1$ , positive  $d_{SSA}$  (black circles in Fig. 6b). On the other hand, for  $AE_{440-870} < 1$ , there is increased

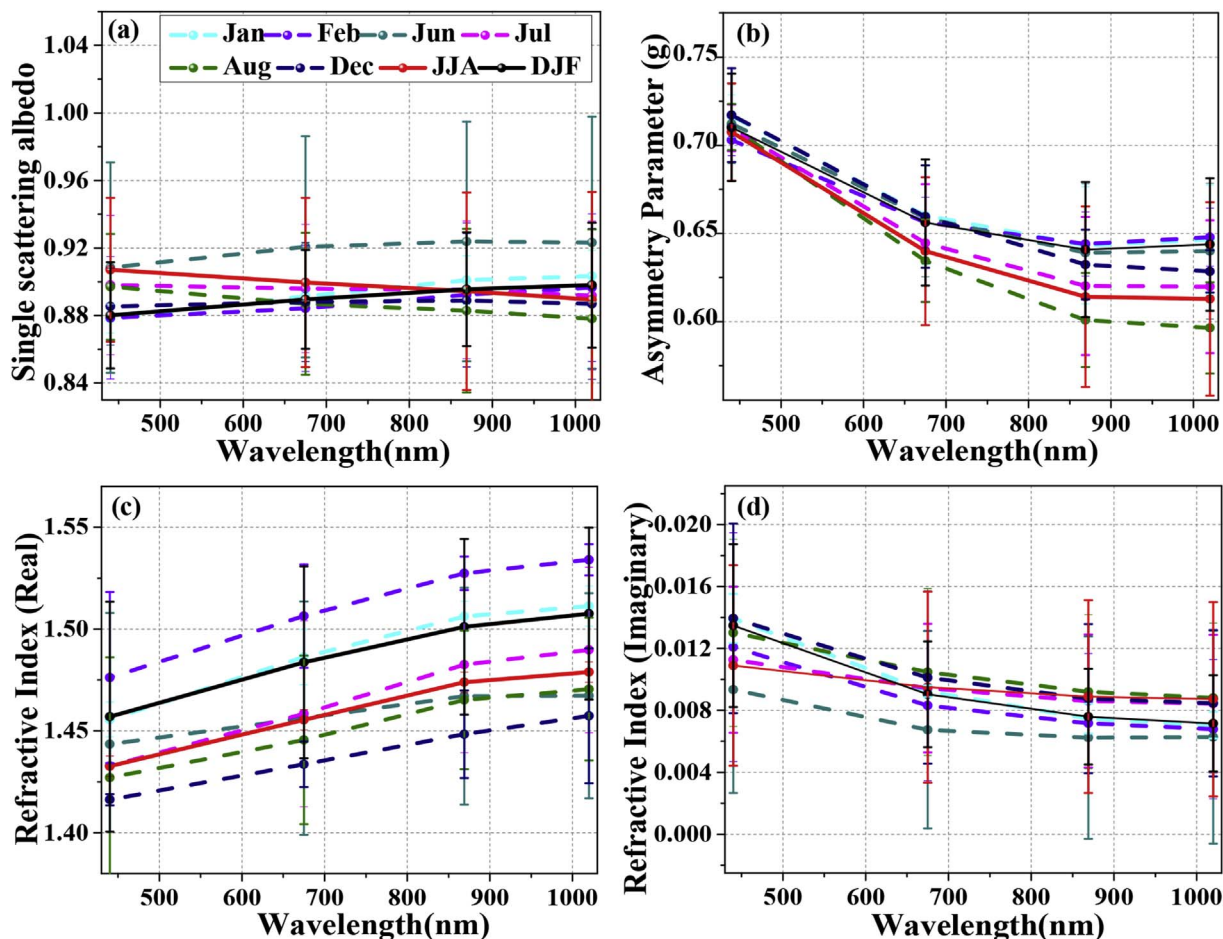


Fig. 9. Spectral variations of (a) single scattering albedo, (b) asymmetry parameter, (c) real, and (d) imaginary parts of refractive indices. The vertical bars indicate  $\pm 1\sigma$  standard deviation of the mean.

absorption at 440 nm, negative  $d_{SSA}$  with significant absorption at 1020 nm (blue and red circles) due to a mixture of dust with anthropogenic aerosols. The extremely low values of  $d_{SSA}$  ( $< -1$ ) suggest dominance of iron oxides likely from dust aerosols (Dumka et al., 2014).

#### 4.7.3. Spectral variations ASY and RI

The asymmetry parameter (ASY) describes the preferred direction of scattering of light interacting with the aerosol particles. It is dependent on the size and composition of the particles and is a key parameter controlling the aerosol contribution to radiative forcing. ASY displayed marked spectral variation, with higher values at shorter wavelengths that consistently decreased in the visible and slightly increased in the near infrared region (Fig. 9b). The averaged ASY during JJA were  $0.71 \pm 0.03$  and  $0.61 \pm 0.05$  at 440 nm and 1020 nm, respectively; whereas, they were found to be  $0.71 \pm 0.03$  and  $0.64 \pm 0.04$  at the respective wavelengths during DJF. Low values of ASY during JJA (with greater decrease in the spectral slope) suggests abundance of anthropogenic aerosols which are absorbing fine-mode particles (Alam et al., 2011, 2012; Yu et al., 2016a, b; Bibi et al., 2017). However, higher values during DJF indicate presence of scattering coarse-mode (mainly dust) over fine-mode absorbing aerosols (Alam et al., 2012).

The optical properties of aerosols are also defined in terms of refractive index (RI), a linear combination of the real (Re) and imaginary (Im) parts. The RI is an important property when considering absorption and scattering of incoming solar radiation by aerosols. Higher values of Re-RI and Im-RI corresponds to scattering and absorbing type of aerosols, respectively (Singh et al., 2004; Alam et al., 2012; Adesina et al., 2014; Kumar et al., 2017). Fig. 9c shows the spectral variations of Re-RI over Mbita for specific months and seasons during which SSA existed. The monthly averaged values of Re-RI ranged from 1.42 to 1.48

and 1.46–1.53 at shorter and longer wavelengths, respectively. Higher ( $> 1.53$ ) values of Re-RI in February and January (and generally DJF) interprets coarse-mode scattering particles; whereas, lower values in June–August (generally JJA) shows presence of fine-mode absorbing particles (Alam et al., 2011, 2012; Che et al., 2013; Yu et al., 2016b).

The spectral variation of Im-RI revealed significant wavelength dependency, decreasing with increasing wavelengths (Fig. 9d). The Im-RI values varied between 0.008 at 1020 nm in December to 0.014 at 440 nm in January. On seasonal basis Im-RI ranged from  $0.011 \pm 0.006$  to  $0.009 \pm 0.006$  at 440 nm during JJA and  $0.013 \pm 0.005$  to  $0.007 \pm 0.003$  at 1020 nm during DJF. Higher values of Im-RI during JJA supports abundance of absorbing aerosols likely from biomass burning activities; whereas, lower values during DJF confirms presence of scattering dust aerosols (Singh et al., 2004; Alam et al., 2011, 2012; Adesina et al., 2017; Iftikhar et al., 2017).

#### 4.8. Aerosol radiative forcing, efficiency, and heating rate

The monthly averaged values of ARF at the TOA, BOA, and ATM along with the corresponding AHR measured at Mbita during the study period are shown in Fig. 10a. The ARF at BOA showed strong variability ( $-24.02$  to  $-58.02 \text{ Wm}^{-2}$ ) compared to the TOA ( $-8.01$  to  $-21.33 \text{ Wm}^{-2}$ ) and ATM ( $2.09$  to  $36.69 \text{ Wm}^{-2}$ ). The annual mean ARF at the TOA, BOA, and ATM during the entire study period were noted to be  $-13.84 \pm 4.63$ ,  $-40.39 \pm 10.13$ , and  $23.77 \pm 11.34 \text{ Wm}^{-2}$ , respectively. The AHR ranged from  $0.06$  to  $1.03 \text{ K day}^{-1}$ , with averaged value of  $0.67 \pm 0.53 \text{ K day}^{-1}$ . The ARF values investigated in the present study are lower than those obtained by a number of authors (see Table 3). Negative BOA forcing indicates a decrease in solar radiation reaching the ground producing a net cooling effect on the Earth's surface. On the other hand, negative TOA forcing shows increase in backscattered light

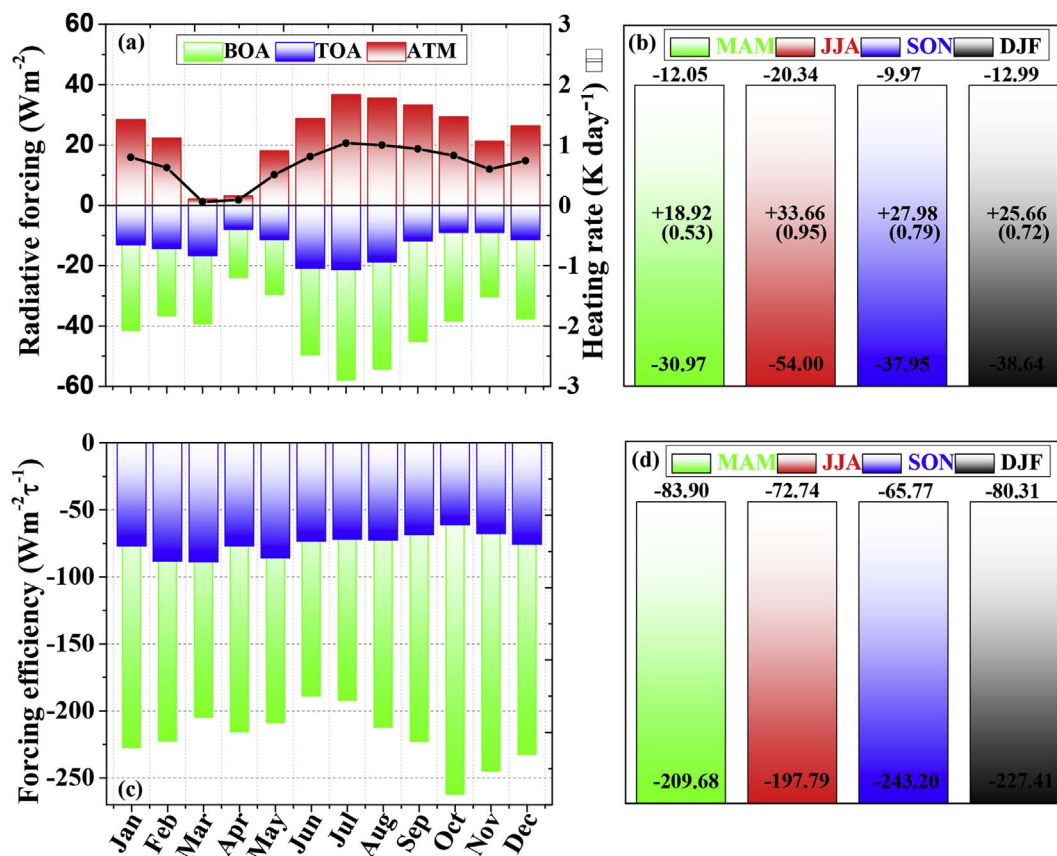


Fig. 10. Monthly variations and seasonal pictorial depiction of direct aerosol radiative forcing (a, b) and forcing efficiency (c, d) at TOA, BOA, and within atmosphere measured over Mbita during 2007–2015.

resulting in cooling of the Earth-atmosphere system. The positive values of ARF within the atmosphere (ATM) suggest significant absorption of solar radiation producing a net warming effect. Largest values of ARF at TOA, BOA, and ATM occurred during JJA with peak values in July. This suggests relatively large abundance of absorbing aerosols (mostly biomass burning), characterized by higher values of AOD and AE (Table 4). Seasonal mean ARF values of  $-12.05$ ,  $-20.34$ ,  $-9.97$  and  $-12.99$   $\text{Wm}^{-2}$  (for TOA),  $-30.97$ ,  $-54.00$ ,  $-37.95$  and  $-38.64$   $\text{Wm}^{-2}$  (BOA) and  $18.92$ ,  $33.66$ ,  $27.98$  and  $25.66$   $\text{Wm}^{-2}$  (ATM) were found during MAM, JJA, SON and DJF, respectively (Fig. 10b). The corresponding values of AHR values were  $0.53$ ,  $0.95$ ,  $0.79$  and  $0.72$   $\text{K day}^{-1}$  during the respective seasons.

The monthly and seasonal evolutions of the aerosol radiative forcing efficiency (ARFE) at BOA and TOA are shown in Fig. 10c and d, respectively. The ARFE during the study period ranged from  $-188.86$   $\text{Wm}^{-2}\tau^{-1}$  to  $262.14$   $\text{Wm}^{-2}\tau^{-1}$  (BOA) and  $-60.94$   $\text{Wm}^{-2}\tau^{-1}$  to  $-88.84$   $\text{Wm}^{-2}\tau^{-1}$  (TOA), with respective mean values of  $-219.52 \pm 20.86$  and  $-75.68 \pm 8.50$   $\text{W m}^{-2}\tau^{-1}$ . The seasonal mean ARFE values of  $-83.90$ ,  $-72.74$ ,  $-65.77$  and  $-80.31$   $\text{W m}^{-2}\tau^{-1}$  (for TOA),  $-209.68$ ,  $-197.79$ ,  $-243.20$  and  $-227.41$   $\text{W m}^{-2}\tau^{-1}$  (BOA), and  $18.92$ ,  $33.66$ ,  $27.98$ ,  $25.66$   $\text{Wm}^{-2}$  (ATM) were noticed at Mbita during MAM, JJA, SON, and DJF, respectively (Fig. 10d).

#### 4.9. Relationship between optical properties and radiative forcing

Fig. 11 shows the relationships between daily averaged aerosol optical properties ( $\text{AOD}_{500 \text{ nm}}$ ,  $\text{AE}_{440-870 \text{ nm}}$ ,  $\text{SSA}_{440 \text{ nm}}$  and  $\text{ASY}_{440 \text{ nm}}$ ) and ARF (at the TOA, BOA and ATM) observed at Mbita. As expected, absolute values of ARF significantly increased with increasing AOD (Fig. 11a). The correlation between ARF and  $\text{AOD}_{500 \text{ nm}}$  at BOA, TOA

and ATM were  $r = -0.88$ ,  $-0.75$ , and  $+0.69$ , respectively (Fig. 11a). The high values of correlations indicate that ARF is a strong function of AOD. A relatively similar pattern was observed for the scatter plot between ARF and  $\text{AE}_{440-870 \text{ nm}}$  (Fig. 11b). At Mbita, ARF at the TOA, BOA, and ATM peaked at  $\text{AE}_{440-870 \text{ nm}} \sim 1.1$ . This shows significant influence of anthropogenic aerosol emissions, particularly during JJA and DJF where  $\text{AE} > 1.0$  (see Table 4).

The ARF also displays linear relationship with other important optical parameters, such as SSA (Fig. 11c) and ASY (Fig. 11d). As expected, lower values of SSA produce greater negative values of ARF at BOA since aerosols with lower SSA absorb more radiation. This could lead to higher ARF and less radiation at BOA, resulting in heating within the ATM and cooling at BOA and TOA. Over Mbita, SSSA and ASY peaked at  $0.85$  and  $0.72$ , respectively, signifying warming effect within the atmosphere likely due to strong absorption caused by smoke and soot particles. It is, therefore, evident that the ARF is a significant source of heating, particularly within the lower atmosphere, increasing the uncertainty of the aerosol effect on regional climate.

#### 4.10. HYSPLIT trajectory analysis

The aerosol load at a particular location is influenced by both emissions and prevailing synoptic meteorological conditions (Kumar et al., 2009; Luo et al., 2014). The meteorological factors (mainly synoptic scale wind circulation patterns) affect air mass transport from source to receptor regions. It is therefore crucial to get prerequisite information on the source regions and transport pathways of aerosols for adequate mitigation measures. In order to ascertain sources and transport pathways of aerosols over Mbita, air mass backward trajectories were computed using the Hybrid Single Particle Lagrangian

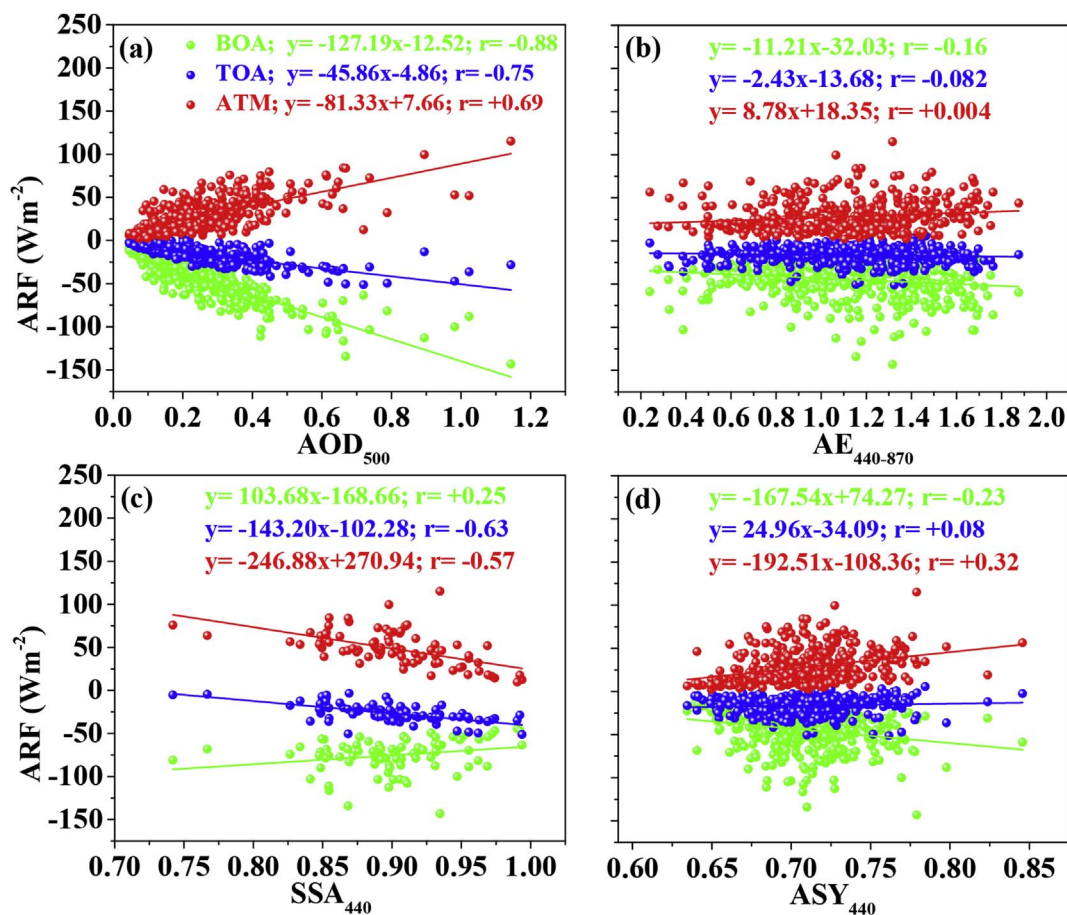


Fig. 11. Relationships between ARF measured at TOA, BOA, and ATM with (a)  $\text{AOD}_{500 \text{ nm}}$ , (b)  $\text{AE}_{440-870 \text{ nm}}$ , (c)  $\text{SSA}_{440 \text{ nm}}$  and (d)  $\text{ASY}_{440 \text{ nm}}$  observed from daily averaged level 2.0 inversion products measured at Mbita. The regression coefficients and Pearson's correlation coefficient ( $r$ ) obtained from the linear regression analysis are also shown in all the panels.



Integrated Trajectory (HYSPPLIT) model (Draxler and Rolph, 2003). The meteorological input for the model were the Global Data Assimilation System (GDAS) dataset reprocessed from the National Centers for Environmental Prediction (NCEP) by Air Resources Laboratory (ARL). A 3-day vertical velocity motion backward air mass trajectories at 1500 m were computed over Mbita for each season during 2011 as a typical representative year for the entire study period (Fig. 12). The 3-day time period was considered sufficient since typical residence time for most aerosols in the lower atmosphere is  $\sim 1$  week (Kumar et al., 2015).

The air mass backward trajectories arriving at Mbita showed significant seasonality in a direction, similar to the findings reported by the previous authors (Gatebe et al., 2001; Ngaina and Muthama, 2014; Boiyo et al., 2017a) over other locations in EA. During MAM and DJF, Mbita experienced significant local anthropogenic activities (land clearing and biomass burning) as well as urban (construction activities) and industrial pollution from the nearby cities. In addition, smoke, dust, and sea-salt particles from Madagascar Island, Sahara and Arabian Deserts, and southwest of Indian Ocean, respectively could significantly increase aerosol load during the two seasons (Fig. 12a, d). It should, however, be noted that low AOD during MAM was attributed to enhanced precipitation, which leads to large wet deposition of aerosols (Fig. 1e). High AOD during JJA is closely associated with air masses of local origin which are responsible for the advection of BUI. In addition, air mass from southwest of Indian Ocean and Madagascar Island (Fig. 12b) could transport significant amount of sea-salt and BB

aerosols, respectively. During SON, the air mass trajectories transport pollutants mainly from Madagascar Island, Indian Ocean, and Arabian Peninsula of varied types. These leads to increased AOD but moderated, by precipitation around the site.

## 5. Conclusions

The optical, microphysical and radiative properties of aerosols have been analyzed over Mbita, a rural site located in Kenya, East Africa using nine years (2007–2015) of ground-based AERONET data. In addition, associated aerosol properties such as source identification, modification process and aerosol type discrimination have been examined. The main findings drawn from the present work are summarized as follows:

1. High (low) values of aerosol optical properties ( $AOD_{500\text{ nm}}$ ,  $AE_{440-675\text{ nm}}$ ,  $FMF_{500\text{ nm}}$ ) were noticed during the local dry (wet) seasons, while CWV showed the converse. The high values of aerosol optical properties during local dry seasons indicate abundance of fine-relative to coarse-mode particles associated with biomass burning and other anthropogenic activities.
2. The spectral AOD and AE was used in deriving the curvature ( $a_2$ ). Negative (positive) curvature characterized aerosol-size dominated by fine (coarse)-mode particles. High negative values of  $a_2$  during JJA attributed to fine-mode biomass burning aerosols.

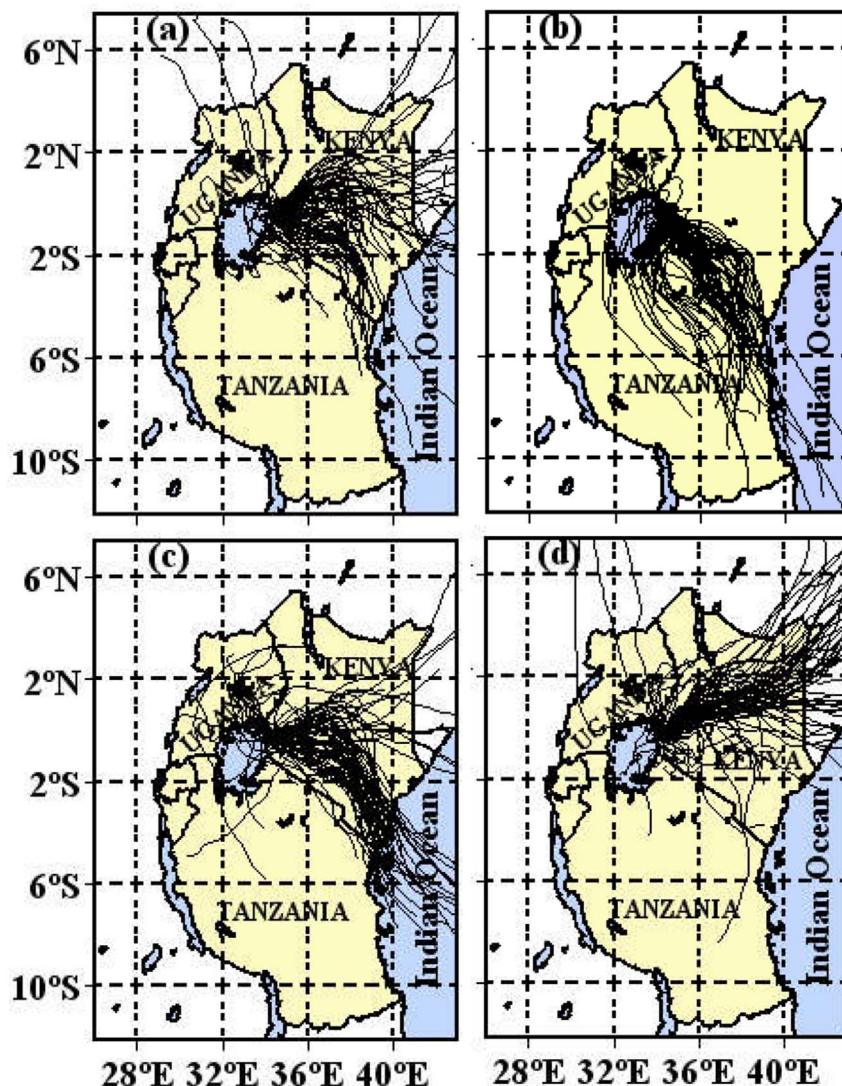


Fig. 12. Air mass backward trajectories arriving at Mbita during (a) MAM, (b) JJA, (c) SON, and (d) DJF for a typical year, 2011. The areas shaded blue represent water bodies, while black capital alphabet labeling represent the three countries constituting EA. (For interpretation of the references to color in this figure legend, the reader is referred to the Web version of this article.)



- Identification of aerosol types using AOD<sub>500 nm</sub> versus AE<sub>440–870 nm</sub> relationship revealed presence of MXD type of aerosols in all seasons, with the highest contribution of 32.81% during JJA. Other aerosol types: BUI, DDT, CMA, and CCB also made the highest contributions of 37.72%, 1.40%, 14.91%, and 13.16%, respectively during JJA. Following the graphical scheme proposed by Gobbi et al. (2007), it is revealed that the increase in AOD<sub>675nm</sub> at Mbita is closely associated with anthropogenic fine- and coarse-mode emissions. The coarse-mode dust particles prevailed in small proportions during most seasons; whereas, fine-mode dominated during JJA.
- The variations in VSD showed a bimodal lognormal structure with a modal peak observed in fine-mode at a geometric mean radius of 0.15 µm and the coarse-mode varied from 3.86 to 5.06 µm. A prominently high volume concentration in fine-mode is evident during JJA suggesting strong loading of anthropogenic aerosols resulting from frequent biomass burning activities.
- The SSA observed over Mbita showed strong spectral dependence generally increasing (decreasing) with increase in wavelength during DJF (JJA) attributed to the dominance of coarse-mode DDT particles (fine mode BUI type) which are scattering (absorbing type) in nature. The ASY also showed spectral dependency with higher values noted at shorter wavelengths that consistently decreased in the visible spectral spectrum and slightly increased in the near infrared region due to the abundance of coarse-mode particles.
- The averaged ARF at TOA, BOA and ATM were  $-13.84 \pm 4.63$ ,  $-40.39 \pm 10.13$  and  $23.77 \pm 11.34$  Wm<sup>-2</sup>, respectively, with resulting averaged AHR of  $0.67 \pm 0.53$  K day<sup>-1</sup>. Large values of ARF at TOA, BOA and ATM together with high AHR during JJA suggest large abundance of absorbing aerosols. The aerosol optical properties (AOD, AE, SSA and ASY) significantly influenced the magnitude of ARF resulting an overall cooling at BOA and TOA and heating at ATM.
- The HYSPLIT model trajectory analysis showed significant seasonal heterogeneity in air masses reaching Mbita. Apart from aerosols of local origin (i.e., biomass burning and industrial-vehicular emissions), the long range transport of aerosols from Saharan and Arabian Deserts, southwest of the Indian Ocean and Madagascar Island resulted in enhanced aerosol loading during the local dry seasons.

## Acknowledgments

This work was financially supported by the National Key R and D Program Pilot Projects of China (Grant no. 2016YFC0203304), the National Natural Science Foundation of China (Grant No. 91644224), and the NUIST Key Laboratory for Aerosol-Cloud-Precipitation of China Meteorological Administration (Grant No. KDW1404). The authors are indebted the Principal Investigator Prof. Brent Holben (NASA) and the staff for their initiative in establishing and maintaining 'ICIPE\_Mbita' AERONET site used in the present study. The lead author Mr. Richard Boiyo extends sincere gratitude to Ministry of Higher Education, Science and Technology of Kenya, Meru University of Information Science and Technology (Kenya) and China Scholarship Council (CSC) for facilitating scholarship during 2015–2018 to pursue Ph.D at NUIST, Nanjing, China. We sincerely thank the NOAA ARL for computing air mass back trajectories using the HYSPLIT model. The meteorological data used in this work were procured from the ECMWF ERA-interim reanalysis, Climate Research Unit (CRU), and TRMM. The authors would like to acknowledge Prof. James Jay Schauer, the U.S. Executive Editor of the Atmospheric Environment Journal and the two anonymous reviewers for their helpful comments and constructive suggestions towards the improvement of an earlier version of the manuscript.

## Appendix A. Supplementary data

Supplementary data related to this article can be found at <http://dx.doi.org/10.1016/j.atmosenv.2018.01.018>.

[doi.org/10.1016/j.atmosenv.2018.01.018](http://dx.doi.org/10.1016/j.atmosenv.2018.01.018).

## References

- Adesina, A.J., Kumar, K.R., Sivakumar, V., Griffith, D., 2014. Direct radiative forcing of urban aerosols over Pretoria (25.75°S, 28.28°E) using AERONET Sunphotometer data: first scientific results and environmental impact. *J. Environ. Sci.* 26, 2459–2474. <https://doi.org/10.1016/j.jes.2014.04.006>.
- Adesina, A.J., Piketh, S., Kumar, K.R., Venkataraman, S., 2017. Characteristics of columnar aerosol optical and microphysical properties retrieved from the sun photometer and its impact on radiative forcing over Skukuza (South Africa) during 1999–2010. *Environ. Sci. Pollut. Res.* 24, 16160–16171. <https://doi.org/http://dx.doi.org/10.1007/s11356-017-9211-2>.
- Alam, K., Tratman, T., Blaschke, T., 2011. Aerosol optical properties and radiative forcing over mega-city Karachi. *Atmos. Res.* 101, 773–782.
- Alam, K., Thomas, T., Thomas, B., Hussain, M., 2012. Aerosol optical and radiative properties during summer and winter seasons over Lahore and Karachi. *Atmos. Environ.* 50, 234–245. <https://doi.org/10.1016/j.atmosenv.2011.12.027>.
- Amiridis, V., Balis, D.S., Kazadzis, S., Bais, A., Giannakaki, E., Papayannis, A., Zerefos, C., 2005. Four-year aerosol observations with a Raman lidar at Thessaloniki, Greece, in the framework of European aerosol Research lidar network (EARLINET). *J. Geophys. Res.* 110, D21203. <http://dx.doi.org/10.1029/2005JD006190>.
- Ångström, A., 1961. Techniques of determining the turbidity of the atmosphere. *Tellus A* 13, 214–223. <https://doi.org/10.1111/j.2153-3490.1961.tb00078>.
- Bibi, H., Alam, K., Bibi, S., 2017. Estimation of shortwave direct aerosol radiative forcing at four locations on the Indo-Gangetic Plains: model results and ground measurement. *Atmos. Environ.* 163, 166–181.
- Bibi, H., Alam, K., Blaschke, T., Bibi, S., Iqbal, M.J., 2016. Long-term (2007–2013) analysis of aerosol optical properties over four locations in the Indo-Gangetic plains. *Appl. Opt.* 55 (23), 6199–6211.
- Boiyo, R., Kumar, K.R., Zhao, T., Bao, Y., 2017a. Climatological analysis of aerosol optical properties over East Africa observed from space-borne sensors during 2001–2015. *Atmos. Environ.* 152, 298–313. <https://doi.org/10.1016/j.atmosenv.2016.12.050>.
- Boiyo, R., Kumar, K.R., Zhao, T., 2017b. Statistical intercomparison and validation of multisensory aerosol optical depth retrievals over three AERONET sites in Kenya, East Africa. *Atmos. Res.* 197, 277–288. <http://doi.org/10.1016/j.atmosres.2017.07.012>.
- Charlson, R.J., Schwartz, S.E., Hales, J.M., Cess, R.D., Coakley, J.A., Hansen, J.E., Hofmann, D.J., 1992. Climate Forcing by Anthropogenic Aerosols Science, vol. 255. pp. 423–430. <http://doi.org/10.1126/science.255.5043.423>.
- Che, H., Zhang, X.Y., Chen, H.B., Damiri, B., Goloub, P., Li, Z.Q., Zhang, X.C., Wei, Y., Zhou, H.G., Dong, F., et al., 2009. Instrument calibration and aerosol optical depth validation of the China aerosol remote sensing network. *J. Geophys. Res.* 114.
- Che, H., Xia, X., Zhu, J., Li, Z., Dubovik, O., Holben, B.N., et al., 2013. Column aerosol optical properties and aerosol radiative forcing during a serious haze-fog month over North China Plain in 2013 based on ground-based Sunphotometer measurements. *Atmos. Chem. Phys.* 14, 2125–2138.
- Che, H., Zhang, X.Y., Xia, X., Goloub, P., Holben, B., Zhao, H., Wang, Y., et al., 2015. Ground-based aerosol climatology of China: aerosol optical depths from the China Aerosol Remote Sensing Network (CARSNET) 2002–2013. *Atmos. Chem. Phys.* 15, 7619–7652.
- Cheng, T., Xu, C., Duan, J., Wang, Y., et al., 2015. Seasonal variation and difference of aerosol optical properties in columnar and surface atmospheres over Shanghai. *Atmos. Environ.* 123, 315–326.
- de Graaf, M., Tilstra, L.G., Aben, I., Stammes, P., 2010. Satellite observations of the seasonal cycles of absorbing aerosols in Africa related to the monsoon rainfall. 1995–2008. *Atmos. Environ.* 44, 1274–1283. <https://doi.org/10.1016/j.atmosenv.2009.12.038>.
- Derimian, Y., Karnieli, A., Kaufman, Y.J., Andreae, M.O., Andreae, T.W., Dubovik, O., et al., 2008. The role of iron and black carbon in aerosol light absorption. *Atmos. Chem. Phys.* 8, 3623–3637. <https://doi.org/10.5194/acp-8-3623-2008>.
- Draxler, R.R., Rolph, G.D., 2003. HYSPLIT (Hybrid Single Particle Lagrangian Integrated Trajectory). Air Resources Laboratory, National Oceanic and Atmospheric Administration, Silver Spring, Md available at: <http://www.arl.noaa.gov/ready/hysplit4.html>.
- Dubovik, O., Holben, B., Eck, T.F., Smirnov, A., Kaufman, Y.J., King, M.D., et al., 2002. Variability of absorption and optical properties of key aerosol types observed in worldwide locations. *J. Atmos. Sci.* 59, 590–608. [http://dx.doi.org/10.1175/1520-0469\(2002\)059<0590:VOAAOP>2.0.CO;2](http://dx.doi.org/10.1175/1520-0469(2002)059<0590:VOAAOP>2.0.CO;2).
- Dubovik, O., Smirnov, A., Holben, B.N., King, M.D., Kaufman, Y.J., Eck, T.F., Slutsker, I., 2000. Accuracy assessments of aerosol optical properties retrieved from Aerosol Robotic Network (AERONET) Sun and sky radiance measurements. *J. Geophys. Res.* 105, 9791. <https://doi.org/10.1029/2000JD900040>.
- Dumka, U.C., Tripathi, S.N., Misra, A., Giles, D.M., Eck, T.F., Sagar, R., Holben, B.N., 2014. Latitudinal variation of aerosol properties from Indo-Gangetic plain to central Himalayan foothills during TIGERZ campaign. *J. Geophys. Res. Atmos.* 119. <https://doi.org/10.1002/2013JD021040>.
- Eck, T.F., Holben, B.N., Reid, J.S., Dubovik, O., Smirnov, A., O'Neill, N.T., et al., 1999. Wavelength dependence of the optical depth of biomass burning, urban, and desert dust aerosols. *J. Geophys. Res.* <https://doi.org/10.1029/1999JD900923>.
- Eck, T.F., Holben, B.N., Siniuk, A., Pinker, R.T., Goloub, P., Chen, H., Chatenet, B., Li, Z., Singh, R.P., Tripathi, S.N., Reid, J.S., Giles, D.M., Dubovik, O., O'Neill, N.T., Smirnov, A., 2010. Climatological aspects of the optical properties of fine/coarsemode aerosol mixtures. *J. Geophys. Res.* 115, D19205.
- El-Metwally, M., Alfaro, S.C., Wahab, M.M.A., Favez, O., Mohamed, Z., Chatenet, B.,

2011. Aerosol properties and associated radiative effects over Cairo (Egypt). *Atmos. Res.* 99, 263–276. <https://doi.org/10.1016/j.atmosres.2010.10.017>.
- Esteve, A.R., Estellés, V., Utrillas, M.P., Martínez-lozano, J.A., 2014. Analysis of the aerosol radiative forcing over a Mediterranean urban coastal site. *Atmos. Res.* 137, 195–204. <https://doi.org/10.1016/j.atmosres.2013.10.009>.
- Gatebe, C.K., Tyson, P.D., Annegarn, H.J., Helas, G., Kinyua, A.M., Piketh, S.J., 2001. Characterization and transport of aerosols over equatorial eastern Africa. *Global Biogeochem. Cycles* 15, 663–672. <https://doi.org/10.1029/2000GB001340>.
- Gauderman, W.J., Connell, R.M., Gilliland, F., London, S., Thomas, D., Avol, E., Vora, H., Berhane, K., Rappaport, E.B., Lurmann, F., Margolis, H.G., Peters, J., 2002. Association between air pollution and lung function growth in southern California children: results from a second cohort. *Am. J. Respir. Crit. Care Med.* 166, 76–84. <https://doi.org/10.1164/rccm.2111021>.
- Giles, D.M., Holben, B.N., Eck, T.F., Sinyuk, A., Smirnov, A., Slutsker, I., et al., 2012. An analysis of AERONET aerosol absorption properties and classifications representative of aerosol source regions. *J. Geophys. Res.* 117. <https://doi.org/10.1029/2012JD018127>.
- Gobbi, G.P., Kaufman, Y.J., Koren, I., Eck, T.F., 2007. Classification of aerosol properties derived from AERONET direct sun data. *Atmos. Chem. Phys. Discuss.* 6, 8713–8726. <https://doi.org/10.5194/acpd-6-8713-2006>.
- Holben, B.N., Eck, T.F., Slutsker, I., Tanré, D., Buis, J.P., Setzer, A., Vermote, J.A., Reagan, J.A., Kaufman, Y.J., Nakajima, T., Jankowiak, Jankowiak, I., Smirnov, A., 1998. AERONET - a federated instrument network and data archive for aerosol characterization. *Remote Sens. Environ.* 66, 1–16. [https://doi.org/10.1016/S0034-4257\(98\)00031-5](https://doi.org/10.1016/S0034-4257(98)00031-5).
- Holben, B.N., Tanre, D., Smirnov, A., Eck, T.F., Slutsker, I., Abuhassan, N., Newcomb, W.W., Schafer, J., Chatenet, B., Lav- enue, F., Kaufman, Y.J., Vande Castle, J., Setzer, A., Markham, B., Clark, D., Froiun, R., Halthore, R., Karnieli, A., O'Neill, N.T., Pietras, C., Pinker, R.T., Voss, K., Zibordi, G., 2001. An emerging ground-based aerosol climatology: aerosol Optical Depth from AERONET. *J. Geophys. Res.* 106, 12067–12097.
- Huffman, G.J., Bolvin, D.T., Nelki, E.J., Wolff, D.B., Adler, R.F., Gu, G., Hong, Y., Bowman, K.P., Stocker, E.F., 2007. The TRMM Multisatellite Precipitation Analysis (TMPA): quasi-global, multiyear, combined-sensor precipitation estimates at fine scales. *J. Hydrometeorol.* 8, 38–55. <https://doi.org/10.1175/JHM560.1>.
- Ifitkhar, M., Alam, K., Sorooshian, A., Syed, W.A., Bibi, S., Bibi, H., 2017. Contrasting aerosol optical and radiative properties between dust and urban haze episodes in megacities of Pakistan. *Atmos. Environ.* 173, 157–172.
- IPCC, 2013. In: Stocker, T.F., Qin, D., Plattner, G.-K.S., Tignor, M., Allen, S.K., Boschung, J., Nauels, A., Xia, Y., Bex, V., Midgley, P.M. (Eds.), *Climate Change 2013: the Physical Science Basis. Contribution of Working Group-I to the Fifth 4 Assessment Report of the Intergovernmental Panel on Climate Change*. 6 Cambridge University Press, Cambridge, United Kingdom And New York, NY, USA, 1535. <https://doi.org/10.1017/CBO9781107415324>.
- Kahn, R., Gaitley, B., Martonchik, J., Diner, D., Crean, K., Holben, B., 2005. MISR global aerosol optical depth validation based on two years of coincident AERONET observations. *J. Geophys. Res.* 110, D10S04. <https://doi.org/10.1029/2004JD00406>.
- Kalluri, R.O.R., Gugamsetty, B., Kotalo, R.G., Nagireddy, S.K.R., Tandule, C.R., Thotli, L.R., Ramakrishna, R.R., Surendranair, S.B., 2016. Direct radiative forcing properties of atmospheric aerosols over semi-arid region, Anantapur in India. *Sci. Total Environ.* 566, 1002–1013.
- Kang, N., Kumar, K.R., Hu, K., Yu, X., Yin, Y., 2016a. Long-term (2002–2014) evolution and trend in Collection 5.1 Level-2 aerosol products derived from the MODIS and MISR sensors over the Chinese Yangtze River Delta. *Atmos. Res.* 181, 29–43. <https://doi.org/10.1016/j.atmosres.2016.06.008>.
- Kang, N., Kumar, K.R., Yu, X., Yin, Y., 2016b. Column-integrated aerosol optical properties and direct radiative forcing over the urban-industrial megacity Nanjing in the Yangtze River Delta, China. *Environ. Sci. Pollut. Control Ser.* 23, 17532–17552. <https://doi.org/10.1007/s11356-016-6953-1>.
- Kaskaoutis, D.G., Badarinath, K.V.S., Kharol, S.K., Sharma, A.R., Kambezidis, H.D., 2009. Variations in the aerosol optical properties and types over the tropical urban site of Hyderabad, India. *J. Geophys. Res.* Atmos. 114 (22), 1–20. <https://doi.org/10.1029/2009JD012423>.
- Kaskaoutis, D.G., Kambezidis, H.D., 2006. Investigation on the wave-length dependence of the aerosol optical depth in the Athens area. *Q. J. R. Meteorol. Soc.* 132, 2217–2234. <https://doi.org/10.1256/qj.05.183>.
- Kaskaoutis, D.G., Kambezidis, H.D., Hatzianastassiou, N., Kosmopoulos, P.G., Badarinath, K.V.S., 2007. Aerosol climatology: dependence of the Angstrom exponent on wavelength over four AERONET sites. *Atmos. Chem. Phys. Discuss.* 7, 7347–7397. <https://doi.org/10.5194/acpd-7-7347-2007>.
- Kaskaoutis, D.G., Kharol, S.K., Sinha, P.R., Singh, R.P., Kambezidis, H.D., Rani Sharma, A., Badarinath, K.V.S., 2011. Extremely large anthropogenic-aerosol contribution to total aerosol load over the Bay of Bengal during winter season. *Atmos. Chem. Phys.* 11, 7097–7117. <https://doi.org/10.5194/acp-11-7097-2011>.
- Kedia, S., Ramachandran, S., Holben, B.N., Tripathi, S.N., 2014. Quantification of aerosol type, and sources of aerosols over the Indo-Gangetic plain. *Atmos. Environ.* 98, 607–619. <https://doi.org/10.1016/j.atmosenv.2014.09.022>.
- Kerandi, N.M., Laux, P., Arnault, J., Kunstmann, H., 2017. Performance of the WRF model to simulate the seasonal and interannual variability of hydrometeorological variables in East Africa: a case study for the Tana River basin in Kenya. *Theor. Appl. Climatol.* <http://doi.org/10.1007/s00704-016-1890-y>.
- Kumar, K.R., Kang, N., Sivakumar, V., Griffith, D., 2017. Temporal characteristics of columnar aerosol optical properties and radiative forcing (2011–2015) measured at AERONET's Pretoria-CSIR DPSS site in South Africa. *Atmos. Environ.* 165, 274–289.
- Kumar, K.R., Sivakumar, V., Reddy, R.R., Gopal, K.R., Adesina, A.J., 2013. Inferring wavelength dependence of AOD and Ångström exponent over a sub-tropical station in South Africa using AERONET data: influence of meteorology, long-range transport and curvature effect. *Sci. Total Environ.* 461–462, 397–408. <https://doi.org/10.1016/j.scitotenv.2013.04.095>.
- Kumar, K.R., Sivakumar, V., Yin, Y., Reddy, R.R., Kang, N., Diao, Y., Yu, X., et al., 2014. Long-term (2003–2013) climatological trends and variations in aerosol optical parameters retrieved from MODIS over three stations in South Africa. *Atmos. Environ.* 95, 400–408. <http://doi.org/10.1016/j.atmosenv.2014.07.001>.
- Kumar, K.R., Yin, Y., Sivakumar, V., Kang, N., Yu, X., Diao, Y., Adesina, A.J., Reddy, R.R., 2015. Aerosol climatology and discrimination of aerosol types retrieved from MODIS, MISR and OMI over Durban (29.88°S, 31.02°E), South Africa. *Atmos. Environ.* 117, 9–18. <https://doi.org/10.1016/j.atmosenv.2015.06.058>.
- Kumar, K.R., Narasimulu, K., Reddy, R.R., Gopal, K.R., Reddy, L.S.S., Balakrishnaiah, G., Moorthy, K.K., Babu, S.S., 2009. Temporal and spectral characteristics of aerosol optical depths in a semi-arid region of southern India. *Sci. Total Environ.* 407, 2673–2688.
- Kumar, S., Sagnik, D., Arun, S., 2016. Quantifying enhancement in aerosol radiative forcing during 'extreme aerosol days' in summer at Delhi National capital region, India. *Sci. Total Environ.* 550, 994–1000. <https://doi.org/10.1016/j.scitotenv.2016.01.191>.
- Liao, W., Wang, X., Fan, Q., Zhou, S., Chang, M., Wang, Z., Tu, Q., et al., 2015. Long-term atmospheric visibility, sunshine duration and precipitation trends in South China. *Atmos. Environ.* 107, 204–216. <http://doi.org/10.1016/j.atmosenv.2015.02.015>.
- Liou, K.N., 2002. *An Introduction to Atmospheric Radiation*. Elsevier, New York, pp. 583.
- Lyamani, H., Olmo, F.J., Alados-Arboledas, L., 2009. Physical and optical properties of aerosols over an urban location in Spain: seasonal and diurnal variability. *Atmos. Chem. Phys. Discuss.* 9, 18159–18199. <https://doi.org/10.5194/acpd-9-18159-2009>.
- Makokha, J.W., Angeyo, H.K., 2013. Investigation of radiative characteristics of the Kenyan atmosphere due to aerosols using sun spectrophotometry measurements and the COART model. *Aerosol Air Quality Res* 201–8. <https://doi.org/http://dx.doi.org/10.4209/aaqr.2012.06.0146>.
- McMichael, A.J., Woodruff, R.E., Hales, S., 2006. Climate change and human health: present and future risks. *Lancet* 367, 859–869. [https://doi.org/10.1016/S0140-6736\(06\)68079-3](https://doi.org/10.1016/S0140-6736(06)68079-3).
- Moorthy, K.K., Babu, S.S., Satheesh, S.K., 2005. Aerosol characteristics and radiative impacts over the Arabian Sea during the intermonsoon season: results from ARMEX field campaign. *J. Atmos. Sci.* 62, 192–206. <http://doi.org/10.1175/JAS-3378.1>.
- More, S., Pradeep, K., Gupta, P., Devara, P.C.S., Aher, 2013. Comparison of aerosol products retrieved from AERONET, MICROTOS and MODIS over a tropical urban city, Pune, India. *Aerosol Air Quality Res.* 13, 107–121. <https://doi.org/http://dx.doi.org/10.4209/aaqr.2012.04.0102>.
- Ngaina, J.N., Muthama, J.M., 2014. Monitoring spatial-temporal variability of aerosol over Kenya. *Ethiopian J. Environ. Stud. Manag.* 7. <https://doi.org/10.4314/ejms.v7i3.2>.
- Ogunjobi, K.O., He, Z., Simmer, C., 2008. *Spectral Aerosol Optical Properties from AERONET Sun-photometric Measurements over West Africa*, vol. 88. pp. 89–107.
- Ogwang, B.A., Chen, H., Li, X., Gao, C., 2016. Evaluation of the capability of RegCM4.0 in simulating east African climate. *Theor. Appl. Climatol.* 124, 303–313.
- O'Neill, N.T., Dubovik, O., Eck, T.F., 2001. Modified Ångström exponent for the characterization of submicrometer aerosols. *Appl. Opt.* 40, 2368–2375.
- Ongoma, V., Chen, H., 2017. Temporal and spatial variability of temperature and precipitation over east africa from 1951 to 2010. *Meteorol. Atmos. Phys.* 129, 131–144. <https://doi.org/10.1007/s00703-016-0462-0>.
- Pace, G., Sarra, A., Meloni, D., Piacentino, S., Chamard, P., 2006. Aerosol optical properties at lampedusa (central mediterranean). Influence of transport and identification of different aerosol types. *Atmos. Chem. Phys. Discuss.* 5, 4929–4969. <http://doi.org/10.5194/acpd-5-4929-2005>.
- Patel, P.N., Dumka, U.C., Kaskaoutis, D.G., Babu, K.N., Mathur, A.K., 2017a. Optical and radiative properties of aerosols over Desalpur, a remote site in western India: source identification, modification processes and aerosol type discrimination. *Sci. Total Environ.* 575, 612–627. <https://doi.org/10.1016/j.scitotenv.2016.09.023>.
- Patel, P.N., Dumka, U.C., Babu, K.N., Mathur, A.K., 2017b. Aerosol characterization and radiative properties over Kavaratti, a remote island in southern Arabian Sea from the period of observations. *Sci. Total Environ.* 599, 165–180. <https://doi.org/10.1016/j.scitotenv.2017.04.168>.
- Pathak, B., Kalita, G., Bhuyan, K., Bhuyan, P., Moorthy, K.K., 2010. Aerosol temporal characteristics and its impact on shortwave radiative forcing at a location in the northeast of India. *J. Geophys. Res.* 115.
- Ramanathan, V., Crutzen, P.J., Kiehl, J.T., Rosenfeld, D., 2001. Aerosols, climate, and the hydrological cycle. *Science* 294, 2119–2124. <http://doi.org/10.1126/science.1064034>.
- Reid, J.S., Eck, T.F., Christopher, S.A., Hobbs, P.V., Holben, B.N., 1999. Use of the Ångström exponent to estimate the variability of optical and physical properties of aging smoke particles in Brazil. *J. Geophys. Res.* 104, 27473–27489.
- Remer, L.A., Kaufman, Y.J., Tanré, D., Mattoo, S., Chu, D.A., Martins, J.V., Li, R.R., Ichoku, C., Levy, et al., 2005. The MODIS aerosol algorithm, products, and validation. *J. Atmos. Sci.* 62, 947–973. <https://doi.org/10.1175/JAS3385.1>.
- Russell, P.B., Bergstrom, R.W., Shinozuka, Y., Clarke, A.D., De Carlo, P.F., Jimenez, J.L., Strawa, a, et al., 2009. Absorption Ångström Exponent in AERONET and related data as an indicator of aerosol composition. *Atmos. Chem. Phys. Discuss.* 9, 21785–21817. <http://doi.org/10.5194/acpd-9-21785-2009>.
- Schuster, G.L., 2005. The Ångström Exponent and Bimodal Aerosol Size Distributions. <https://doi.org/10.1029/>.
- Singh, R.P., Dey, S., Tripathi, S.N., Tare, V., Holben, B., 2004. Variability of aerosol parameters over Kanpur, northern India. *J. Geophys. Res.: Atmospheres* 109, 1–14. <https://doi.org/10.1029/2004JD004966>.
- Smirnov, A., Holben, B.N., Dubovik, O., O'Neill, N.T., Eck, T.F., Westphal, D.L., et al.,

2002. Atmospheric aerosol optical properties in the Persian Gulf. *J. Atmos. Sci.* 59, 620–634. <https://doi.org/10.1175/1520>.
- Tiwari, S., Tiwari, S., Hopke, P.K., Attiri, S.D., Soni, V.K., Singh, A.K., 2016. Variability in optical properties of atmospheric aerosols and their frequency distribution over a mega city “New Delhi”, India. *Environ. Sci. Pollut. Res.* 23, 8781–8793.
- Welton, E.J., Campbell, J.R., 2002. Micropulse lidar signals: uncertainty analysis. *J. Atmos. Ocean. Technol.* 9, 2089–2094. [http://dx.doi.org/10.1175/1520-0426\(2002\)](http://dx.doi.org/10.1175/1520-0426(2002)).
- Yang, W., Seager, R., Cane, M.A., Lyon, B., 2015. The annual cycle of East African precipitation. *J. Clim.* 28, 2385–2404. <https://doi.org/10.1175/JCLI-D-14-00484.1>.
- Yu, X., Kumar, K.R., Lü, R., Ma, J., 2016a. Changes in column aerosol optical properties during extreme haze-fog episodes in January 2013 over urban Beijing. *Environ. Pollut.* 210, 217–226. <https://doi.org/10.1016/j.envpol.2015.12.021>.
- Yu, X., Lu, R., Kumar, K.R., Ma, J., Zhang, Q., Jiang, Y., Kang, N., Yang, S., Wang, J., Li, M., 2016b. Dust aerosol properties and radiative forcing observed in spring during 2001–2014 over urban Beijing, China. *Environ. Sci. Pollut. Res.* 23, 15432–15442.
- Luo, Y., Zheng, X., Zhao, T., Chen, J., 2014. A climatology of aerosol optical depth over China from recent 10 year of MODIS remote sensing data. *Int. J. Climatol.* <http://dx.doi.org/10.1002/joc.3728>.
- Zhang, J., Reid, J.S., 2010. A decadal regional and global trend analysis of the aerosol optical depth using a data-assimilation grade over-water MODIS and Level 2 MISR aerosol products. *Atmos. Chem. Phys.* 10, 10949–10963.